WIDE INPUT RANGE DC-DC CONVERTER WITH DIGITAL CONTROL SCHEME

A Thesis

by

MAJA HARFMAN TODOROVIC

Submitted to the Office of Graduate Studies of
Texas A&M University
in partial fulfillment of the requirements for the degree of

MASTER OF SCIENCE

December 2004

Major Subject: Electrical Engineering

WIDE INPUT RANGE DC-DC CONVERTER WITH DIGITAL CONTROL SCHEME

A Thesis

by

MAJA HARFMAN TODOROVIC

Submitted to Texas A&M University
in partial fulfillment of the requirements
for the degree of

MASTER OF SCIENCE

Approved as to style and content by:

Prasad Enjeti (Chair of Committee)	
Hamid Toliyat (Member)	Anthony J. Appleby (Member)
Shankar Bhattacharyya (Member)	Chanan Singh (Head of Department)

December 2004

Major Subject: Electrical Engineering

ABSTRACT

Wide Input Range DC-DC Converter with Digital Control Scheme.

(December 2004)

Maja Harfman Todorovic, B.S., University of Belgrade, Serbia and Montenegro

Chair of Advisory Committee: Dr. Prasad Enjeti

In this thesis analysis and design of a wide input range DC-DC converter is proposed along with a robust power control scheme. The proposed converter and its control is designed to be compatible to a fuel cell power source, which exhibits 2:1 voltage variation as well as a slow transient response. The proposed approach consists of two stages: a primary three-level boost converter stage cascaded with a high frequency, isolated boost converter topology, which provides a higher voltage gain and isolation from the input source. The function of the first boost converter stage is to maintain a constant voltage at the input of the cascaded DC-DC converter to ensure optimal performance characteristics with high efficiency. At the output of the first boost converter a battery or ultracapacitor energy storage is connected to take care of the fuel cell slow transient response (200 watts/min). The robust features of the proposed control system ensure a constant output DC voltage for a variety of load fluctuations, thus limiting the power being delivered by the fuel cell during a load transient. Moreover, the proposed configuration simplifies the power control management and can interact with the fuel cell controller. The simulation results and the experimental results confirm the feasibility of the proposed system.

DEDICATION

To my love Milos.

ACKNOWLEDGEMENTS

I would like to express my gratitude to my advisor, Dr. Prasad Enjeti, for his technical and theoretical support, guidance and encouragement throughout my graduate studies. I would like to thank all my committee members for their help, time and concern. Also, I would like to thank all my fellow students working in the Power Electronics and Power Quality Laboratory at Texas A&M University, especially Leonardo Palma, Chuttchaval Jeraputra, and Prabha Acharya for their help and guidance.

Most of all, I am grateful to my husband Milos for his love, support and encouragement.

TABLE OF CONTENTS

Page

CHAPTER Page

LIST OF FIGURES

Page

Page

Page

Page

LIST OF TABLES

Page

CHAPTER I
INTRODUCTION

1.1 Introduction

Most of the present electric power demand in the world is met by fossil and nuclear power plants. In recent years, we have witnessed a steadily growing interest in ecologically clean and renewable energy technologies, such as the fuel cells, wind and solar power plants.

The wind is a free, clean, and inexhaustible energy source. It has served humankind well for many centuries by propelling ships and driving wind turbines to grind grain and pump water. Denmark was the first country to use wind for generation of electricity. In addition to home wind-electric generation, a number of utilities around the world have built larger wind turbines to supply power to their customers. There are four distinct categories of wind power plants. Those are:

- small, non-grid connected
- small, grid connected
- large, non-grid connected
- large, grid connected

By small, we mean a size appropriate for an individual to own, rated for up to a few tens of kilowatts. Large refers to utility scale power plants.

This thesis follows the style and format of *IEEE Transactions on Industry Applications.*

Photovoltaic (PV) systems perform the direct conversion of sunlight into electricity with no intervening heat engine. PV devices are solid state; therefore, they are rugged and simple in design and require very little maintenance. A key advantage of the PV systems is that they can be constructed as either grid connected or stand-alone to produce outputs from microwatts to megawatts. They have been used as the power sources for calculators, watches, water pumping, remote buildings, communications, satellites and space vehicles, as well as megawatt-scale power plants. Because they are lightweight, modular, and do not require a gaseous or liquid fuel supply, PVs fit a niche that is unavailable to other DC technologies. These silicon PV cells come in several varieties. The most common cell is the single-crystal silicon cell. Other variations include multicrystalline (polycrystalline), thin silicon cells with buried contact, and amorphous silicon cells.

The United States Department of Energy (DOE) has identified the fuel cell as a distributed energy technology that will soon be participating in the energy market in wide variety of applications including micro-power, central, auxiliary, and transportation systems, stationary power for buildings and other distributed generation applications. A fuel cell is an electrochemical device that produces a DC voltage from the hydrogen-rich fuel gas and air that flow over two cell electrodes. It is similar to conventional battery in that both produce a direct current by using an electrochemical process, and to combustion engine in that both will work continuously as long as the fuel (reactants) are supplied. Main difference between the fuel cell and battery is that the fuel cell is not the energy storage element that needs energy from an external source for recharging purposes.

Fuel cells can be classified in different categories, depending on the type of electrolyte, the temperature of operation, the combination of the fuel and oxidant,

whether the fuel is processed outside or inside the fuel cell, whether the reactants are fed to the cell by internal or external manifolds, etc. The most common classification is by the type of electrolyte used in the cells and includes:

- polymer electrolyte fuel cell (PEFC),
- alkaline fuel cell (AFC),
- phosphoric acid fuel cell (PAFC),
- molten carbonate fuel cell (MCFC),
- solid oxide fuel cell (SOFC).

Although the electrolyte is the primary mean of characterizing the cell, the operating temperature also plays an important role. There are low-temperature operating fuel cells (PEFC, AFC, PAFC) and high-temperature operating fuel cells (MCFC, SOFC); in latter type the temperature is high enough so that the reforming processing of fuel, such as natural gas, occurs within the cell. This internal reforming benefits the system's efficiency because there is an effective transfer of heat from the exothermic cell reaction to satisfy the endothermic reforming reaction. As a result, an external reformer can be removed, which improves the efficiency and reduces the cost of the system. This makes them particularly attractive for fuel-efficient stationary generation. On the other hand, the complexity of the cell increases, thus yielding the higher maintenance requirements.

Typical output voltage of an individual cell has very small values, under 1.2V. Therefore, similar to batteries, individual cells must be combined to produce considerable voltage levels needed for some applications.

1.2 Fuel cell applications

Presently there are many uses for fuel cells; for example all of the major automakers are working to commercialize a fuel cell car. Fuel cells are powering buses, boats, trains, plains, scooters, and even bicycles. There is a variety of commonly used machines powered by fuel cells, such as vending machines, vacuum cleaners, and high road signs. Miniature fuel cells for cellular phones, laptop computers and portable electronics are on their way to the market. Hospitals, credit card centers, police stations, and banks are all using fuel cells to provide power for their facilities. Wastewater treatment plants and landfills are using fuel cells to convert the methane gas they produce into electricity. The possibilities are endless. Main fuel cells applications can be divided into the following categories:

- stationary,
- residential,
- transportation,
- portable power,
- landfill/wastewater treatment.

More than 2500 fuel cell stationary systems have been installed all over the world — in hospitals, nursing homes, hotels, office buildings, schools, utility power plants, and airport terminals, providing primary power or backup [1]. In has been estimated that in large-scale building systems, fuel cells can reduce facility energy service costs by 20% to 40% over conventional energy service.

Fuel cells are ideal for residential power generation, either connected to the electric grid to provide supplemental power and backup assurance for critical areas, or installed

as grid-independent generators for on-site service in areas that are inaccessible by power lines. Since fuel cells operate silently, they reduce noise pollution as well as air pollution and the waste heat from a fuel cell can be used to provide hot water or space heating for a house. Many of the prototypes being tested and demonstrated for residential use extract hydrogen from propane or natural gas [2].

All major automotive manufacturers have a fuel cell vehicle either in development or in testing right now, and Honda and Toyota [3, 4] have already begun leasing vehicles in California and Japan. Automakers and experts speculate that the fuel cell vehicle will not be commercialized until at least 2010; nevertheless, manufacturers started incorporating fuel cells into buses, locomotives, airplanes, scooters and golf carts.

Miniature fuel cells, once available to the commercial market, will help consumers talk for up to a month on a cellular phone without recharging. Fuel cells will change the telecommuting world, powering laptops and palm pilots hours longer than present day batteries. Other applications for micro fuel cells include pagers, video recorders, portable power tools, and low power remote devices such as hearing aids, smoke detectors, burglary alarms, hotel locks, and meter readers [5]. These miniature fuel cells generally run on methanol, an inexpensive wood alcohol.

Fuel cells currently operate at landfills and wastewater treatment plants across the country, proving to be the valid technology for reducing pollution emission and generating power from the methane gas they produce [6].

1.3 Fuel cell plant description

Fuel cells produce DC power, water and heat from the combination of hydrogen produced from the fuel and oxygen from the air. In procedures where CO and CH_4 react in the cell to produce hydrogen, CO_2 is also a co-product. Reactions in fuel cells depend substantially on the temperature and pressure inside the cell. A system must be built around the fuel cell to supply air and clean fuel, convert the energy to a more usable form such as grid quality ac power, and remove the depleted reactants and heat that are produced by the reactions in the cells [7]. Figure 1 shows the basic structure of a fuel cell power plant.

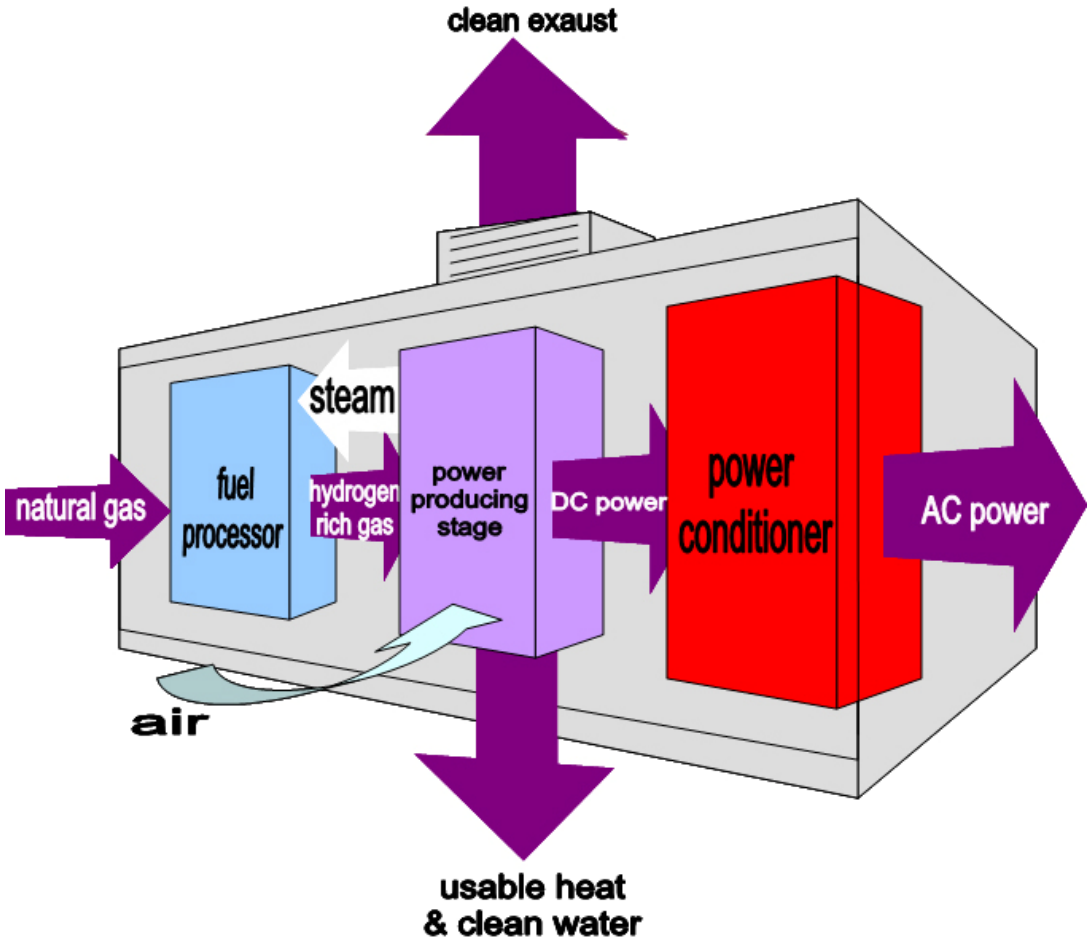

Fig. 1. Block diagram of a fuel cell power system.

First stage of a fuel cell power system plant is a fuel processing unit where a conventional fuel (natural gas, methanol, coil, naphtha, or other gaseous hydrocarbon) is purified into a gas containing hydrogen. The following stage converts chemical energy to DC electricity using the stacks of individual fuel cells. Number of stacks used in the power producing section unit depends on the specific power application. Finally, power conditioner converts DC power generated by the fuel cell stacks into the regulated AC or DC power suitable for customer usage.

1.4 Fuel cell power conditioning system

As shown before, fuel cells have broad spectrum of applications which require a particular power conditioning system. Majority of conditioning systems include DC-to-DC and DC-to-AC power conversion blocks. Since the DC voltage generated by a fuel cell stack varies widely and is low in magnitude (Figure 2) (<60 V for a 5-10 kW system, <350 V for a 300 kW system), a step-up DC-DC conversion stage is essential to generating a higher regulated DC voltage (400 V typical for 120/240 V AC output). The DC to DC converter stage draws power from the fuel cell and should be designed to match the fuel cell's current ripple specifications. Additionally, the DC-DC converter should not introduce any negative current into the fuel cell. Following this stage, a DC-AC inverter is used to supply the AC power at 60 Hz or 50 Hz. An output LC filter stage is connected to produce a low total harmonic distortion (THD) AC waveform.

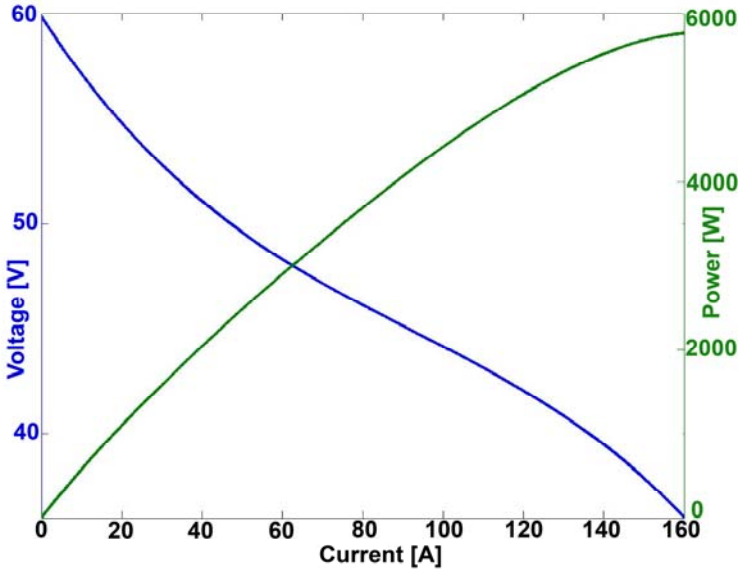

Fig. 2. V-I and P-I curves of a typical SOFC fuel cell.

The primary concern of this thesis is residential applications, or more specifically a conditioner for fuel cell systems supplying dedicated/stand-alone loads. Typical system requirements for these types of applications are continuous 5-10 kW output power, an output AC voltage of 120/240 V at 50/60 Hz, output THD < 5%, efficiency > 90%, etc. Figure 3 shows a block diagram of a typical residential fuel cell system incorporating an auxiliary energy storage device (ultracapacitor or battery) for sudden load changes or fuel-cell start-up.

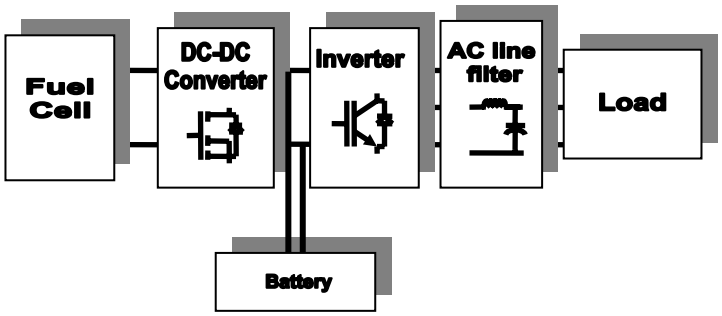

Fig. 3. Block diagram of the complete system.

1.5 Previous work

Selection of the appropriate topology for the DC-DC converter in fuel cell systems depends mainly on the type of the load, type of the auxiliary device (energy storage element), and required transient response. Due to the nature of the fuel supply process, the cell response time to changes in power demand is high and varies from few seconds to a minute. Therefore, it is necessary to improve the dynamics of the system by introducing auxiliary devices. There are several proposed solutions using bidirectional DC-DC converters for charging/discharging the auxiliary battery packs or other energy storage devices [8-11]. Wang *et al.* [8] evaluated different setups using current-fed and voltage-fed half bridge and full bridge converters. Pagano and Piegari [9] focused on the possibility of selecting between a battery and ultracapacitor energy storage device with reference to their features in terms of electrical and reliability aspects. Liu *et al.* [10] presented an interleaved DC-DC converter with small capacitor to minimize input current ripple and they used analog voltage and current controller to maximize fuel cell output power. Bertoni *et al.* [11] used buck/boost topologies for bidirectional converters and investigated the performance of two series structures.

The increase in efficiency was a primary concern of several studies [12-14]. Andersen *et al.* [12] used the current-fed push pull converter; Scheble *et al.* [13] used the soft switching DC-DC converter with auto transformer; and Hernando *et al.* [14] used the full-bridge converter.

1.6 Research objective

The objective of this thesis is to develop a new fuel cell inverter topology with DSP control for residential applications. This involves the analysis and design of a wide input range DC-DC converter along with a robust power control scheme. The proposed converter and its control will be designed to be compatible with a fuel cell power source, which typically exhibits 2:1 voltage variation at its output terminals, as well as a slow transient response. The proposed approach consists of two stages: a conventional boost converter stage cascaded with a DC-DC converter with high frequency isolation, which has a higher voltage gain and isolation from the input source. The function of the first boost converter stage will be to maintain a constant voltage at the input of the cascaded DC-DC converter to ensure optimal performance characteristics with high efficiency. Three different configurations will be considered and analyzed in order to find the one that would best fit our needs. Preliminary studies suggest that the best choice for the first stage power conditioner is likely the parallel three-level configuration. The proposed converter will be designed and generally tested by means of computer simulations. Later on, an experimental prototype will be built and tested for various operating conditions.

At the output of the first boost converter a battery or ultracapacitor energy storage will be connected to take care of the fuel cell slow transient response. The robust features of the proposed control system will ensure a constant output DC voltage for a variety of load fluctuations, thus limiting the power being delivered by the fuel cell during a load transient. Moreover, the proposed configuration will simplify the power control management and will have a possibility to interact with the fuel cell controller. The simulation results and the experimental results will be obtained to prove the feasibility of

the proposed system. The system is tested with the ultracapacitor and with the battery bank to obtain results for systems with different system dynamics. Fuel cell simulator will be used to obtain behavior of the system for different fuel cell sources. Control schemes will be implemented using TMS320LF2407 digital signal processor (DSP) to verify the proposed control schemes.

1.7 Thesis outline

Chapter I of the thesis presents an overview of the fuel cell systems and applications. It briefly describes typical fuel cell plants and their constituent parts such as fuel processors, power conversion stages, and conditioners. More attention is given to fuel cell conditioners for residential applications. Major part of the chapter is devoted to presenting an overview of the current technologies. Finally the research objectives of this work are presented.

Chapter II is devoted to an in depth explanation of different fuel cell technologies and their most important characteristics. A comparison between the various fuel cell types is made.

Chapter III involves the analysis and design of different DC-DC topologies suitable for fuel cell converters. From this analysis, a comparison between different converter topologies is made and a conclusion which topology to use is drawn.

Chapter IV discusses the robust features of the digital control system that ensures a constant output DC voltage for a variety of load fluctuations, thus limiting the power being delivered by the fuel cell during a load transient and fuel cell start-up. Proposed system simulation results with ultracapacitor and with battery bank are presented.

Chapter V presents the experimental results obtained using the 2 kW laboratory prototype. The system was tested under different load conditions and with both the ultracapacitor and the battery as the auxiliary device.

Chapter VI concludes this thesis by presenting the general conclusion of this work.

CHAPTER II
REVIEW OF FUEL CELL SYSTEMS

2.1 Introduction

In 1839, a British jurist and an amateur physicist named William Grove first discovered the principle of the fuel cell by reversing the water electrolysis to generate electricity from hydrogen and oxygen. Grove utilized four large cells, each containing hydrogen and oxygen, to produce electricity and water which was then used to split water in a different container to produce hydrogen and oxygen. However, it took another 120 years until NASA demonstrated its use to provide electricity and water for some early space flights. Today the fuel cell is the primary source of electricity on the space shuttle. As a result of these successes, industry slowly began to appreciate the commercial value of fuel cells. In addition to stationary power generation applications, there is now a strong push to develop fuel cells for automotive use. Even though fuel cells provide high performance characteristics, reliability, durability, and environmental benefits, a very high investment cost is still the major barrier against large-scale deployment.

2.2 Fuel cell operation

Different types of fuel cells can be characterized by the electrolyte used and they are listed in Table I with their main features. All of these fuel cells function in the same basic way. A schematic representation of the fuel cell functionality is shown in Figure 4.

Table I Currently developed types of fuel cells and their characteristics and applications

Fuel Cell Type	Proton exchange membrane FC **PEMFC**	Alkaline FC **AFC**	Phosphoric acid FC **PAFC**	Molten carbonate FC **MCFC**	Solid oxide FC **SOFC**
Electrolyte	Solid polymer (such as Nafion)	KOH	Phosphoric acid	Lithium and potassium carbonate	Solid oxide electrolyte (yttria, zirconia)
Charge carrier	H^+	OH^-	H^+	CO_3^{2-}	O^{2-}
Fuel	Pure H_2 (tolerates CO_2)	Pure H_2	Pure H_2 (tolerates CO_2, approx. 1% CO)	H_2, CO, CH_4, other hydrocarbons (tolerates CO_2)	H_2, CO, CH_4, other hydrocarbons (tolerates CO_2)
Catalyst	Platinum	Platinum	Platinum	Nickel	Perovskites
Operation temperature	50–100°C	60–120°C	~220°C	~650°C	~1000°C
External reformer for CH_4	Yes	Yes	Yes	No	No
Product water management	Evaporative	Evaporative	Evaporative	Gaseous Product	Gaseous Product
Product heat management	Process Gas + Independent Cooling Medium	Process Gas + Electrolyte Circulation	Process Gas + Independent Cooling Medium	Internal Reforming + Process Gas	Internal Reforming + Process Gas
Electric efficiency	35–45%	35–55%	38%-45%	50%-60%	40%-55%
Power range /Application	Automotive, CHP (5–250kW), portable	<5 kW, military, space	CHP (200 kW)	200 kW–MW range, CHP and standalone	2 kW–MW range, CHP and standalone

At the anode, a fuel (usually hydrogen) is oxidized into electrons and protons, and at the cathode, oxygen is reduced to oxide species. Depending on the electrolyte, either protons or oxide ions are transported through the ion-conducting, but electronically

insulating, electrolyte to combine with oxide ions or protons, respectively, to generate water and electric power.

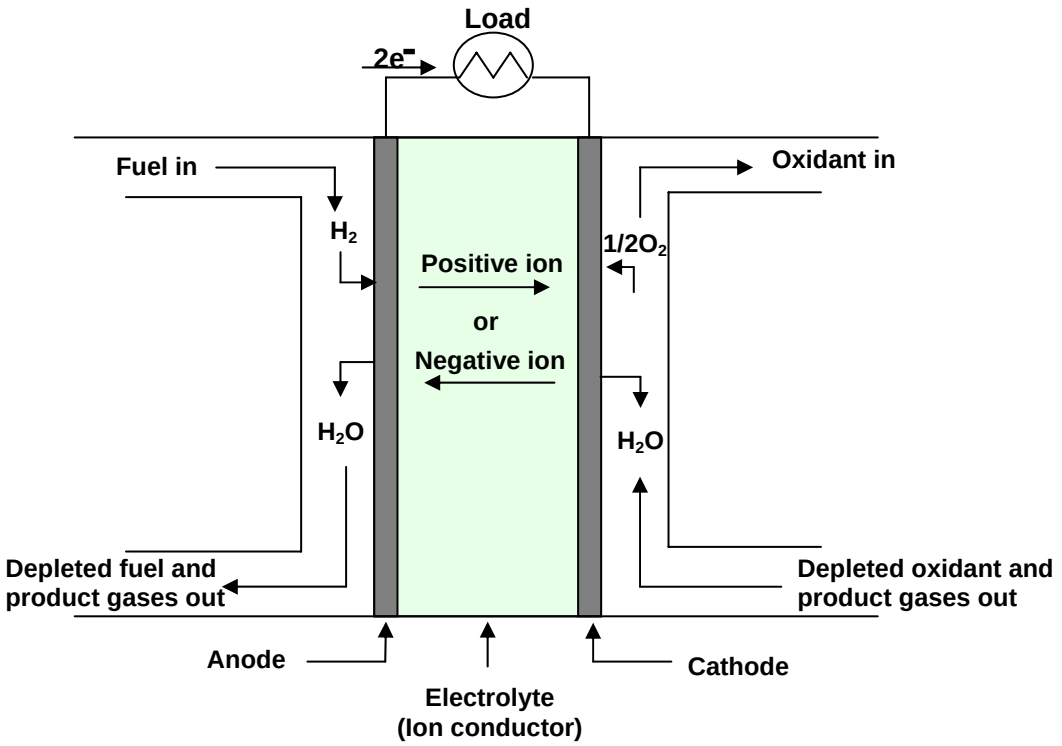

Fig. 4. Fuel cell diagram.

Basic operational characteristics of the five most common types of fuel cells are discussed in the following subchapters.

2.3 Polymer electrolyte membrane fuel cell

The Polymer Electrolyte Membrane Fuel Cell (PEMFC) is one in a family of fuel cells that are in various stages of development. It is being considered as an alternative power source for automotive applications for electric vehicles. The electrolyte in this fuel

cell is an ion exchange membrane (fluorinated sulfonic acid polymer or other similar polymer) that is an excellent proton conductor. Polymer electrolyte membranes are somewhat unusual electrolytes in that, in the presence of water, which the membrane readily absorbs, the negative ions are rigidly held within their structure. Only the positive (H^+) ions contained within the membrane are mobile and are free to carry positive charges through the membrane in one direction only, from anode to cathode. At the same time, the organic nature of the polymer electrolyte membrane structure makes it an electron insulator, forcing it to travel through the outside circuit providing electric power to the load. Each of the two electrodes consists of porous carbon to which very small platinum (Pt) particles are bonded. The electrodes are somewhat porous so that the gases can diffuse through them to reach the catalyst. Moreover, as both platinum and carbon conduct electrons well, they are able to move freely through the electrodes. Chemical reactions that take place inside a PEMFC fuel cell are presented in the following:

$$\begin{aligned} &\text{Anode:} && 2H_2 \rightarrow 4H^+ + 4e^- \\ &\text{Cathode:} && O_2 + 4H^+ + 4e^- \rightarrow 2H_2O \\ &\text{Net reaction:} && 2H_2 + O_2 = 2H_2O\,. \end{aligned} \tag{1}$$

Hydrogen gas diffuses through the polymer electrolyte until it encounters a Pt particle in the anode. The Pt catalyzes the dissociation of the hydrogen molecule into two hydrogen (H) atoms bonded to two neighboring Pt atoms. Only then can each H atom release an electron to form a hydrogen ion (H^+) which travels to the cathode through the electrolyte. At the same time, the free electron travels from the anode to the cathode

through the outer circuit. At the cathode the oxygen molecule interacts with the hydrogen ion and the electron from the outside circuit to form water.

The only liquid in this fuel cell is water; thus, corrosion problems are minimal. Water management in the membrane is critical for efficient performance; the fuel cell must operate under conditions where the byproduct water does not evaporate faster than it is produced because the membrane must be hydrated. Because of the limitation on the operating temperature imposed by the polymer, usually less than 120°C, and because of problems with water balance, a H_2-rich fuel is used. Higher catalyst loading (Pt in most cases) than that used in PAFCs is required for both the anode and cathode. Because carbon monoxide (CO) "poisons" the catalyst, the fuel may contain no CO. PEMFC generates electric power at cell voltages up to 1 V and power densities of up to about 1 Wcm^{-2} as can be seen from Figure 5 [15].

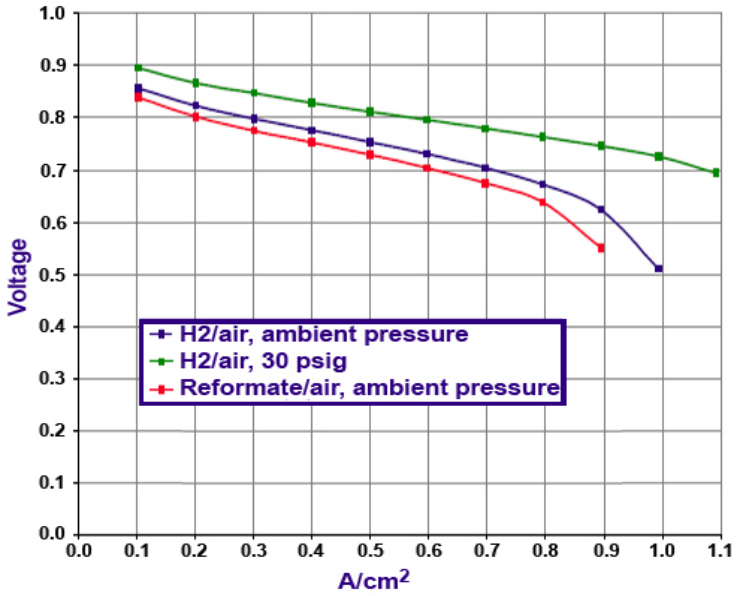

Fig. 5. Polarization curves for 3M 7-layer MEA [15].

The performance of the PEM fuel cell is limited primarily by the slow rate of the oxygen reduction half-reaction at the cathode, which is 100 times slower than the hydrogen oxidation half-reaction at the anode. Besides that, operating temperature has a significant influence on PEMFC performance. An increase in temperature decreases the ohmic resistance of the electrolyte and reduces mass transport limitations. Operation at higher temperatures also reduces the chemisorption of CO. Improving the cell performance through an increase in temperature, however, is limited by the vapor pressure of water in the ion exchange membrane due to the membrane's susceptibility to dehydration and the subsequent loss of ionic conductivity.

Operating pressure also impacts the cell performance. An increase in the pressure of oxygen results in a significant reduction in polarization at the cathode. Performance improvements due to increased pressure must be balanced against the energy required to pressurize the reactant gases. The overall system must be optimized according to output, efficiency, cost, and size.

The PEMFC are attractive for transportation applications, portable power and are a major competitor for stationary power applications less than 100 kW, particularly in combined heat and power (CHP) generation.

No doubt one of the most elegant solutions to the fueling problem would be to make fuel cells operate on a liquid fuel. This is particularly so for transportation and the portable sector. The direct methanol fuel cell (DMFC), a liquid- or vapor-fed PEMFC operating on a methanol/water mix and air deserves careful consideration. The main technological challenges are the formulation of the better anode catalysts to lower the anode over-potentials (currently several hundred mV at practical current densities), and

the improvement of membranes and cathode catalysts in order to overcome cathode poisoning and fuel losses by migration of methanol from anode to cathode. This limitation has prompted a large research effort to search for efficient methanol oxidation catalyst materials — yet it appears that only platinum-based materials show reasonable activity and the required stability. The performances of DMFCs are now in a range that seems feasible for small portable applications; as a consequence, this type of application has been identified as a niche market, which the DMFC could dominate because of reduced system complexity.

2.4 Alkaline fuel cell

The alkaline fuel cell (AFC) was one of the first modern fuel cells to be developed, beginning in 1960. The application at that time was to provide on-board electric power for the Apollo space vehicle. Attractive attributes of the AFC include excellent performance compared to other candidate fuel cells due to its active O_2 electrode kinetics and flexibility to use a wide range of electrocatalysts. This type of fuel cells continues to be used to present days; it now provides on-board power for the Space Shuttle Orbiter.

The half-cell reactions of the alkaline fuel cell are:

$$\text{Anode:} \qquad H_2 + 2OH^- \rightarrow 2H_2O + 2e^-$$

$$\text{Cathode:} \qquad \frac{1}{2}O_2 + H_2O + 2e^- \rightarrow 2OH^- \qquad (2)$$

Hydroxyl ions (OH^-) are the conducting type in the electrolyte. The equivalent overall cell reaction is:

$$H_2 + \frac{1}{2}O_2 \rightarrow H_2O + electric\,energy + heat \quad (3)$$

Since potassium hydroxide (KOH) has the highest conductance among the alkaline hydroxides, it is the preferred electrolyte. There are two types of electrolyte concentration: one is with the very concentrated KOH (85%) and very high operation temperature (~250 °C); another one uses less concentrated KOH (35-50 %) for lower temperature (<120 °C) operation. The electrolyte is retained in a matrix (usually asbestos) and, as mentioned, a wide range of electrocatalysts can be used (e.g., Ni, Ag, metal oxides, spinels, and noble metals) to promote the reaction. The fuel supply is limited to non-reactive constituents except for hydrogen. CO is the poison, and CO_2 reacts with the KOH to form K_2CO_3, thus reducing the electrolyte's ion mobility. Even the small amount of CO_2 in the air is harmful to the alkaline cell. Therefore, gas purification is necessary when H_2 is produced from carbon-containing fuel sources (e.g., methanol, gasoline, propane and others). There are many approaches to separate CO_2 from gaseous or liquid streams. Physical separation and chemical separation are the most common methods used.

However, CO_2 removal by these methods requires more than one processing step to reduce the CO_2 to the limits required by the fuel cell. As a reference, Figure 6 [16] shows the degradation in AFC electrode potential with reformed fuels containing CO_2 and from the presence of CO_2 in air.

As in the case of PAFCs, voltage obtained from an AFC is affected by ohmic, activation and concentration losses.

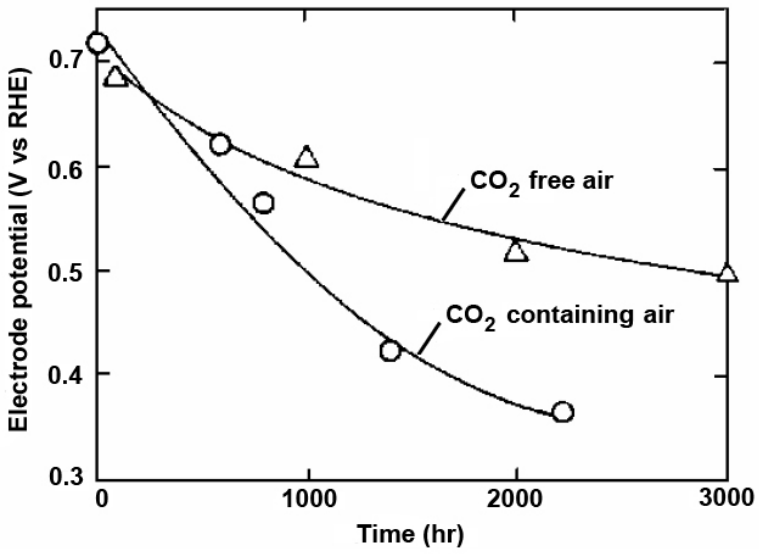

Fig. 6. Degradation in AFC electrode potential with CO_2-containing and CO_2-free air.

Source: Ref. [16], p.381.

The early AFCs operated at relatively high temperature and pressure to meet the requirements for space applications. More recently, a major focus of the technology is for the terrestrial applications in which low-cost components operating at near-ambient temperature and pressure with air as the oxidant are desirable. This shift in fuel cell operating conditions resulted in the lower performance.

2.5 Phosphoric acid fuel cell

The phosphoric acid fuel cell (PAFC) was the first technology moved from the laboratory research to the first stages of commercial application. The PAFC has been developed mainly for the medium-scale power generation market. Turnkey 200 kW plants are now available and have been installed at more than 70 sites in the U.S., Japan, and Europe. Operating at about 200 °C, the PAFC plant also produces heat for domestic

hot water and space heating, and its electrical efficiency approaches 40%. The principal obstacle against widespread commercial acceptance is cost. The electrolyte used in PAFC is the phosphoric acid (H3PO4) concentrated to 100%. At lower temperatures, phosphoric acid is a poor ionic conductor, and CO poisoning of the Pt electrocatalyst in the anode becomes severe. In addition, the use of concentrated acid (100%) minimizes the water vapor pressure so water management in the cell is not difficult. The matrix universally used to retain the acid is silicon carbide, and the electrocatalyst in both the anode and cathode is Pt. The chemical reactions occurring at two electrodes are written as follows:

$$\begin{aligned} &\text{Anode:} && 2H_2 \rightarrow 4H^+ + 4e^- \\ &\text{Cathode:} && O_2 + 4H^+ + 4e^- \rightarrow 2H_2O \end{aligned} \tag{4}$$

The overall cell reaction is:

$$\frac{1}{2}O_2 + H_2 \rightarrow H_2O \tag{5}$$

Although pressurization increased efficiency (lower fuel cost), it complicated the power unit, resulting in higher capital cost. The economic trade-off favored simpler, atmospheric operation for early commercial units. Another important issue, independent of power unit size, is that pressure promotes corrosion.

Typical PAFCs generally operate in the range of 100-400 mA/cm^2 at 600-800 mV/cell. Voltage and power constraints arise from increased corrosion of platinum and carbon components at cell potentials above approximately 800 mV.

Although its cell performance is somewhat lower than the alkaline cell because of the cathode's slow oxygen reaction rate, and although the cell still requires hydrocarbon fuels to be reformed into a H_2-rich gas, the PAFC system efficiency improved because of its higher temperature environment and less complex fuel conversion (no membrane and attendant pressure drop). An increase in temperature has a beneficial effect on cell performance because activation polarization, mass transfer polarization, and ohmic losses are reduced. The kinetics for the reduction of oxygen on Pt improves as the cell temperature increases.

The need for scrubbing CO_2 from the processed air is also eliminated. The rejected heat from the cell is hot enough to heat water or air in a system operating at atmospheric pressure. Some steam is available in PAFCs, a key point in expanding cogeneration applications. PAFC systems achieve about 37 to 42% electrical efficiency which is the low end of the efficiency goal for fuel cell power plants. PAFCs use high cost precious metal catalysts such as platinum, and the fuel has to be reformed externally to the cell. These limitations have prompted development of the alternate, higher temperature cells, MCFC and SOFC. Figure 7 [17] is provided as a reference for PAFC performances at ambient pressure and at 8.2 atm.

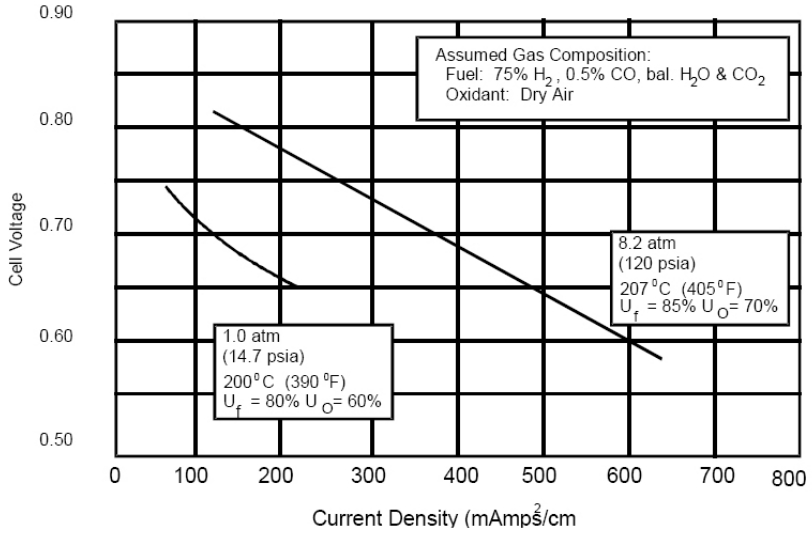

Fig. 7. Reference performance at 8.2 atm and ambient pressure. Cells from full size power plant [17].

2.6 Molten carbonate fuel cell

Molten carbonate technology is attractive because it offers several potential advantages over PAFC. Carbon monoxide, which poisons the PAFC, is indirectly used as a fuel in the molten carbonate fuel cell (MCFC). The higher operating temperature of approximately 650 °C makes the MCFC a better candidate for combined cycle applications whereby the fuel cell exhaust can be used as the input to the intake of a gas turbine or the boiler of a steam turbine. The total thermal efficiency can approach 85%. The electrolyte in this fuel cell is usually a combination of alkali carbonates, typically Li_2CO_3 and K_2CO_3, which is retained in a ceramic matrix of $LiAlO_2$

The high temperature induces the alkali carbonates to form a highly conductive molten salt, with carbonate ions providing ionic conduction. At the high operating temperatures in MCFCs, Ni (anode) and nickel oxide (cathode) are adequate to promote

reaction. The cell reactions occur with nickel catalysts rather than with expensive precious metal catalysts. This high operation temperature allows the reforming to take place within the cell, which results in a large efficiency gain. Typical MCFCs will generally operate in the range of 100 to 200 mA/cm2 at 750 to 900 mV/cell. The data in Figure 8 [18] illustrate the progress that has been made in the performance of single cells, and in the cell voltage of small stacks at 650 °C.

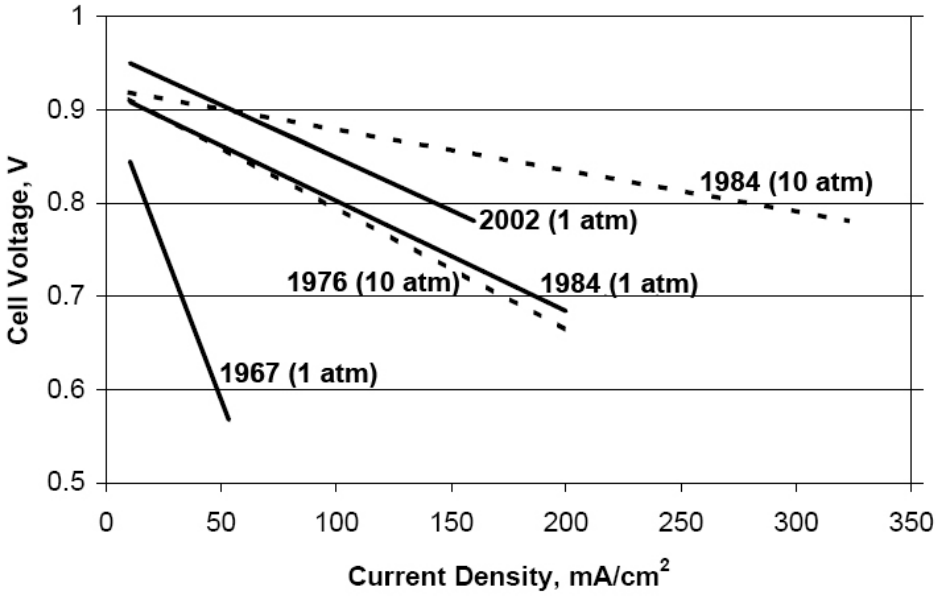

Fig. 8. Progress in the generic performance of MCFC's on reformat gas and air [18].

This technology is at the stage of prototype commercial demonstrations and is estimated to enter the commercial market in the next several years using natural gas, and by 2010 with gas made from coal. Capital costs are expected to be lower than PAFC. MCFCs are now being tested in full-scale demonstration plants. The following equations illustrate the chemical reactions that take place inside the cell.

Anode: $2H_2 + 2CO_3^{2-} \rightarrow 2H_2O + 2CO_2 + 4e^-$

$2CO + 2CO_3^{2-} \rightarrow 4CO_2 + 4e^-$ (6)

Cathode: $O_2 + 2CO_2 + 4e^- \rightarrow 2CO_3^{2-}$

The MCFCs have some disadvantages: the electrolyte is very corrosive and mobile, and a source of CO_2 is required at the cathode (usually recycled from anode exhaust) to form the carbonate ion. Sulfur tolerance is controlled by the reforming catalyst and is low, which is the same for the reforming catalyst in all cells. Operation requires use of stainless steel as the cell hardware material. The higher temperatures promote material problems, particularly mechanical stability that impacts durability.

2.7 Solid oxide fuel cell

A solid oxide fuel cell (SOFC) is currently being demonstrated at a 100 kW plant. Solid oxide technology requires very significant changes in the structure of the cell, which can be cast into flexible shapes, such as tubular, planar, or monolithic. As the name implies, the SOFC uses a solid electrolyte, a ceramic material usually Y_2O_3-stabilized ZrO_2, so the electrolyte does not need to be replenished during the operational life of the cell. This simplifies design, operation, and maintenance, as well as having the potential to reduce costs. Furthermore, it offers the stability and reliability of all solid-state construction and allows higher temperature operation. At the temperature of presently operating SOFCs (~1000 °C), fuel can be reformed within the cell.

The high temperature of the SOFC has its drawbacks. There are thermal expansion mismatches among materials, and sealing between cells is difficult in the flat plate configurations. The high operating temperature places severe constraints on materials selection and results in difficult fabrication processes. The SOFC also exhibit a high electrical resistivity in the electrolyte, which results in a lower cell performance than the MCFC by approximately 100 mV.

The ceramic make-up of the cell lends itself to cost-effective fabrication techniques. The tolerance to impure fuel streams make SOFC systems especially attractive for utilizing H_2 and CO from natural gas steam-reforming and coal gasification plants. The chemical reactions inside the cell may be written as follows:

$$\begin{aligned} &\text{Anode:} && 2H_2 + 2O^{2-} \rightarrow 2H_2O + 4e^- \\ & && 2CO + 2O^{2-} \rightarrow 2CO_2 + 4e^- \\ & && CH_4 + 4O^- \rightarrow 2H_2O + CO_2 + 8e^- \qquad (7) \\ &\text{Cathode:} && O_2 + 4e^- \rightarrow 2O^{2-} \end{aligned}$$

The cell operates at 600-1000 °C where ionic conduction by oxygen ions takes place. Typically, the anode is Co-ZrO_2 or Ni-ZrO_2 cermet, and the cathode is Sr-doped $LaMnO_3$. As seen from Figure 9 [19], high power densities (e.g., 0.9 W/cm2 at 650°C) have been achieved at temperatures less than 650 °C.

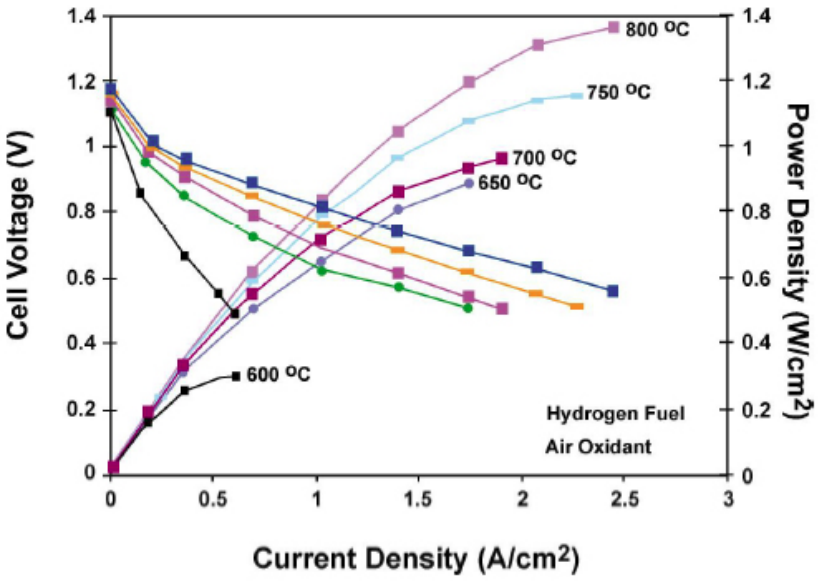

Fig. 9. Performance of SOFC at reduced temperature [19].

In a SOFC, there is no liquid electrolyte present that is susceptible to movement in the porous electrode structure, and electrode flooding is not a problem. Consequently, the three-phase interface that is necessary for efficient electrochemical reaction involves two solid phases (solid electrolyte/electrode) and a gas phase. The kinetics of the cell is fast, and CO is a directly useable fuel as it is in the MCFC. A critical requirement of porous electrodes for SOFC is that they are sufficiently thin and porous to provide an extensive electrode/electrolyte interface for electrochemical reaction.

2.8 Comparison between fuel cells

The fuel cell types described in previous subchapters have significantly different operating regimes. As a result, their hardware materials, fabrication techniques, and system requirements differ. These distinctions result in individual advantages and

disadvantages that govern the potential of the various cells to be used for different applications.

The PEMFC, like the SOFC, have a solid electrolyte. In contrast to the SOFC, the PEMFC cell operates at a low temperature of approximately 80 °C. This result in a capability to bring the cell to its operating temperature quickly, but the rejected heat cannot be used for cogeneration or additional power. The PEMFC can operate at very high current densities compared to the other cells. However, heat and water management issues may limit the operating power density of a practical system. The PEMFC have problem with CO poisoning of the catalyst but increasing the temperature can solve this problem to some extent.

The most advantageous characteristics of the AFC include its excellent performance on hydrogen (H_2) and oxygen (O_2) compared to other fuel cells due to its active O_2 electrode kinetics and its flexibility to use a wide range of electrocatalysts. Disadvantage of the AFC is in that the strongly alkaline electrolytes (NaOH, KOH) adsorb CO_2, which ultimately reduces electrolyte conductivity. This means that impure H_2 containing CO_2 cannot be used as a fuel, and air has to “scrubbed” free of CO_2 prior to use as the oxidant in an AFC.

The PAFC cathode's slow oxygen reaction rate cause lower cell performance than the AFC and the cell still requires hydrocarbon fuels to be reformed into a H_2-rich gas. The PAFC system efficiency improved because of its higher operation temperature and simple fuel conversion (no membrane and attendant pressure drop). Also the need for scrubbing CO_2 from the process air is eliminated.

Two high-temperature fuel cells, (SOFC and MCFC), have two major advantages over low-temperature types. First, they can achieve high electric efficiencies which make them particularly attractive for fuel efficient stationary power generation. Second, the high operating temperatures allow direct internal processing of fuels such as natural gas. This reduces the system's complexity compared with low-temperature power plants, which require hydrogen generation in an additional process step. The PAFC and PEMFC units tend to use precious metal catalysts, while catalysts of the MCFC and SOFC units are typically nickel based, which tremendously reduces the cost. In addition, higher-temperature fuel cells can electrochemically react with hydrogen as well as other fuels (e.g., CO and CH_4).

Table II Ideal voltage as a function of cell temperature under 1 atm pressure

Temperature	25°C	80°C	100°C	205°C	650°C	1000°C
Cell Type		PEMFC	AFC	PAFC	MCFC	SOFC
Ideal Voltage	1.23	1.17		1.14	1.03	0.91

The ideal performance of a fuel cell depends on the electrochemical reactions that occur between different fuels and oxygen as summarized in Table II under the pressure of 1 atm [7]. Low-temperature fuel cells (PEFC, AFC, and PAFC) require noble metal electrocatalysts to achieve practical reaction rates at the anode and cathode, and H_2 is the only acceptable fuel. With high-temperature fuel cells (MCFC and SOFC), the requirements for catalysis are relaxed, and the number of potential fuels expands. While carbon monoxide "poisons" a noble metal anode catalyst such as platinum (Pt) in low

temperature fuel cells, it competes with H_2 as a reactant in high-temperature fuel cells where non-noble metal catalysts such as nickel (Ni) can be used.

2.9 Conclusion

Fuel cells can convert a remarkably high proportion of the chemical energy in a fuel to electricity. With the efficiencies approaching 60%, even without co-generation, fuel cell power plants are nearly twice as efficient as conventional power plants. Unlike large steam plants, the efficiency is not a function of the plant size for fuel cell power plants. Small-scale fuel cell plants are just as efficient as the large ones, whether they operate at full load or not. Fuel cells contribute significantly to the cleaner environment; they produce dramatically fewer emissions, and their by-products are primarily hot water and carbon dioxide in small amounts. Because of their modular nature, fuel cells can be placed at or near load centers, resulting in savings of transmission network expansion.

CHAPTER III
REVIEW OF DC/DC CONVERTERS FOR POWER CONDITIONER UNIT

3.1 Introduction

Power conditioning is an important technology necessary for converting the DC electrical power generated by a fuel cell into usable AC power for stationary loads, automotive applications, and interfaces with electric utilities. The electrical characteristics of a fuel cell are given in Figure 2 showing that they are not an ideal electric power source. A typical fuel cell stack has a DC output voltage that varies widely (2:1) with the load current and age of the fuel cell, and has a limited overload capability. Therefore, a DC-DC converter stage is often required to increase and regulate the fuel cell voltage to higher voltage levels for further processing into AC via a DC-AC inverter stage. In this section, several DC-DC converter topologies are examined that can be engaged in fuel cell systems. These topologies have different performance and complexity and it is very important to select the right converter in order to achieve the maximum utilization of the fuel cell energy and to minimize loses. A survey of the main advantages and disadvantages of the suitable topologies is presented in the following subchapters.

3.2 Boost converter

The boost converter is a well known switched-mode converter that is capable of producing a DC output voltage higher in amplitude than the input DC voltage. The schematic of the boost converter is shown in Figure 10.

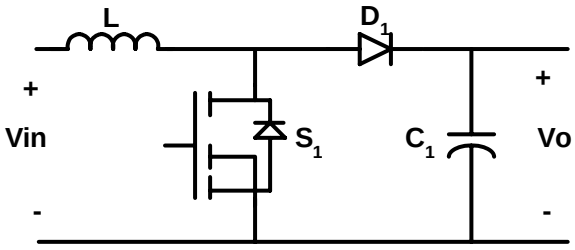

Fig. 10. Topology of the boost converter.

Applying the principles of the inductor volt-second balance and capacitor charge balance we can calculate the steady state output voltage and the inductor current. The gating signal of the switch S_1 (usually MOSFET or IGBT) is a high frequency PWM signal, which produces two operating modes.

The first operating mode shown in Figure 11 is when the switch S_1 is on for a time $t_{on}=DT_s$, D_1 is reverse biased and current ramps up linearly in the inductor L to its peak value. During this period, the energy is stored in the inductor while the output current is supplied entirely from C_1, which is chosen large enough to supply the load current for the time t_{on} with minimum specified drop. In the defining equation for t_{on}, D represents duty cycle and T_s is a switching period. The inductor voltage and capacitor current for this mode are given by:

$$\begin{aligned} v_L &= V_{in} \\ i_C &= -\frac{V_o}{R} \end{aligned} \tag{8}$$

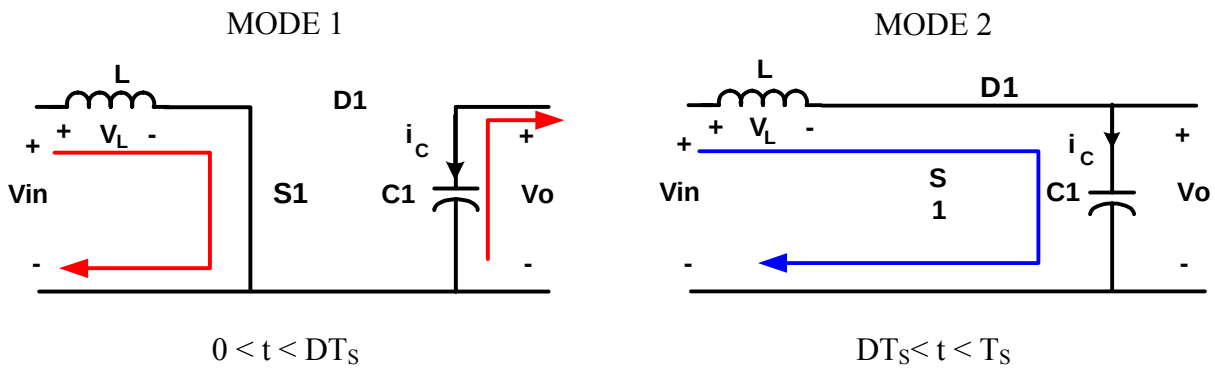

Fig. 11. Boost converter operation modes.

The second operating mode is when the switch S_1 turns off for a time $t_{off} = T_s - t_{on}$. Since the current in an inductor can not change instantaneously, the current in L reverses in an attempt to maintain the current constant. Inductor L delivers its stored energy to the capacitor C and charges it up via diode D_1 to a higher voltage than V_{in}. This energy supplies the load current and replenishes the charge drained away from C when it was supplying the load current. During this period the energy is stored in the capacitor. The inductor voltage and capacitor current for this mode are given by:

$$v_L = V_{in} - V_o$$
$$i_C = i_L - \frac{V_o}{R} \qquad (9)$$

The total volt-seconds applied to the inductor over one switching period are:

$$\int_0^{T_S} v_L(t)dt = V_{in}DT_S + (V_{in} - V_o)\cdot(1-D)T_s. \qquad (10)$$

By equating the equation (10) to zero and collecting the terms, the output voltage becomes:

$$V_o = \frac{V_{in}}{1-D}. \tag{11}$$

This yields the voltage conversion ratio M(D) of the output to the input voltage of

$$M(D) = \frac{V_o}{V_{in}} = \frac{1}{1-D}. \tag{12}$$

Previous equation shows that the output voltage is controlled by the value of the duty cycle and, ideally, the boost converter is capable of producing any voltage higher than the input voltage. There are, of course, the limits to the output voltage that can be produced by a practical boost converter. Practical converter exhibits power losses due to losses in the inductor, diode and the switch. These losses can be properly modeled with a resistor in series with an inductance. This would change the voltage conversion ratio to

$$M(D) = \frac{V_o}{V_{in}} = \frac{1}{1-D} \cdot \frac{1}{\left(1 + \frac{R_L}{(1-D)^2 R}\right)}, \tag{13}$$

where R_L represents losses and R is the load. Voltage conversion ratio for both cases is plotted in Figure 12.

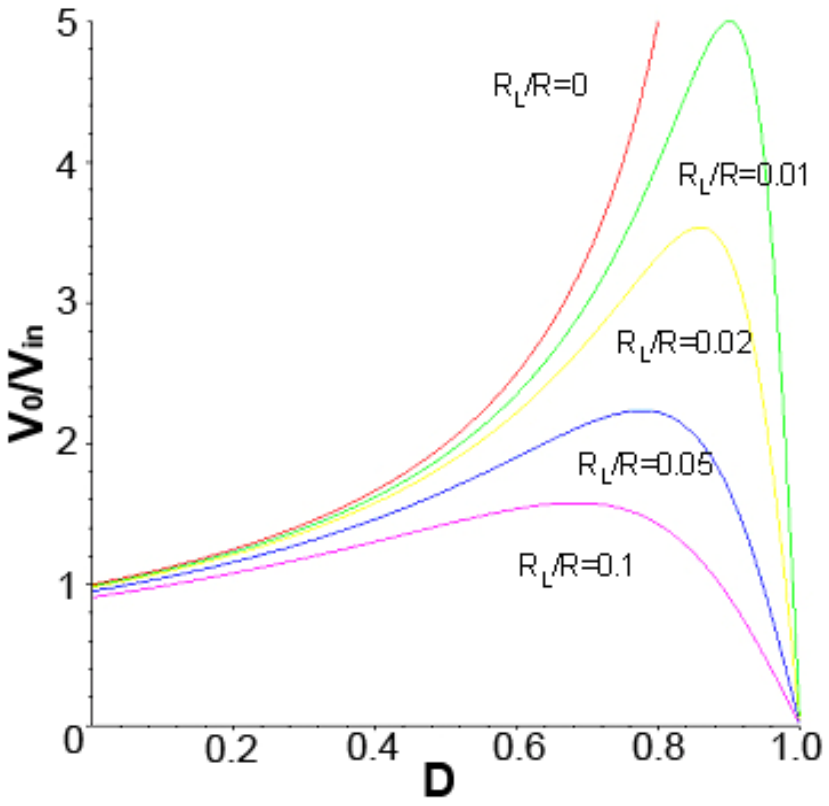

Fig 12. Output voltage vs. duty cycle, boost converter with copper loss.

For cases when the output voltage requirements are higher than the two or three times the input voltage, the use of this topology is not appropriate because of the reduced efficiency and the non-linear characteristic of the voltage gain of the converter, as can be observed in Figure 12. An important characteristic of this topology is that it does not need transformers and the voltage stress for the switch is relatively low when compared to other DC-DC step-up converter topologies. The use of this topology to step up the voltage supplied by fuel cells is feasible when the ratio between the output voltage and the input voltage is not higher than two or three and when no galvanic insulation is required.

3.3 Three-level single-ended boost converter

The three-level boost converter is shown in Figure 13. This converter has two switches, two diodes, and two capacitors at the output, to form the voltage divider. Therefore, the voltage of the center point is $\frac{V_o}{2}$, which is obtained by choosing the C_1=C_2 and the symmetrical operation of the two switches.

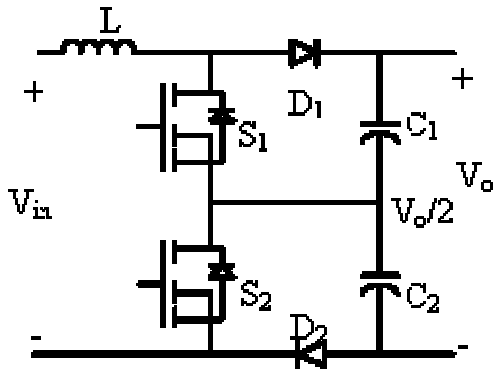

Fig. 13. Three-level boost converter.

There are two regimes where this converter can operate, depending on whether the input voltage is lower or higher than half of the output voltage.

In the first regime ($V_{in} < V_o/2$), the boost inductor charges in modes 1 and 3 (Figure 14), and the output is supplied from the energy stored in the output capacitors. The inductor voltage and capacitor current for this mode are given by

$$\begin{aligned} v_L &= V_{in} \\ i_C &= -\frac{V_o}{R}. \end{aligned} \tag{14}$$

In modes 2 and 4 inductor L delivers its stored energy to the capacitor C_1 via diode D_1 and to the capacitor C_2 via diode D_2, respectively, thus charging them up to a higher voltage than V_{in}.

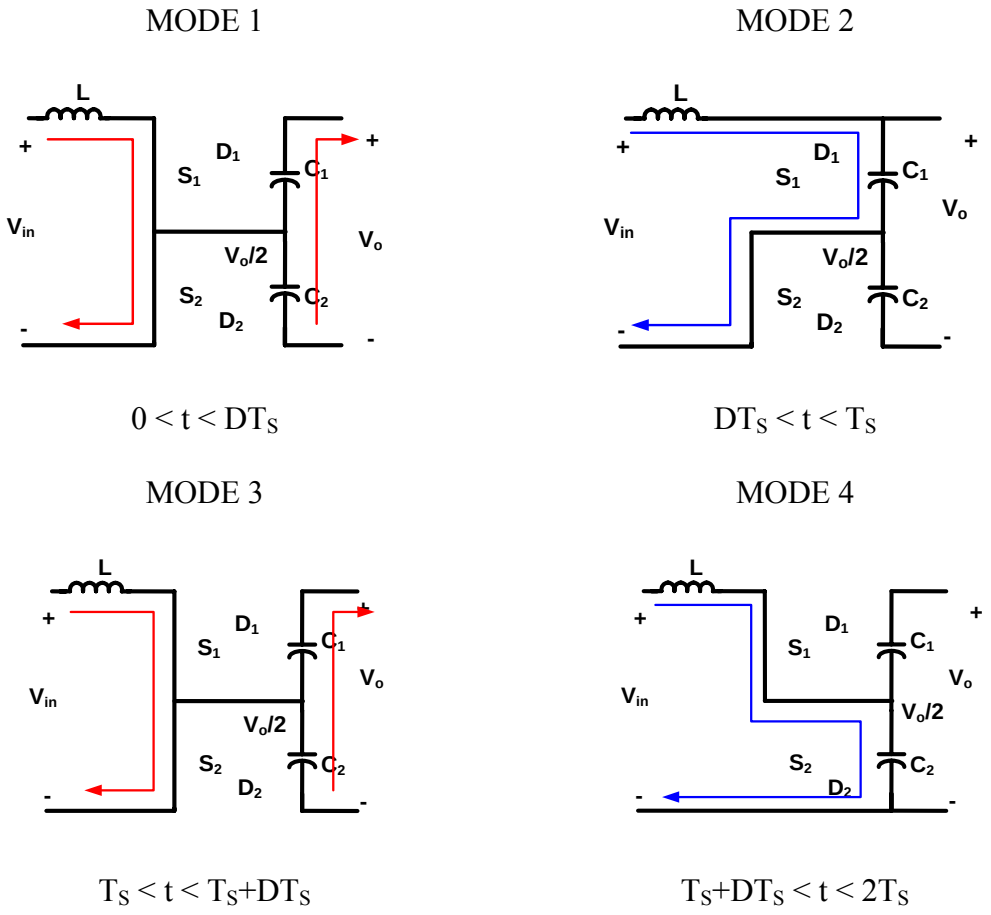

Fig. 14. First section operation modes.

This energy supplies the load current and replenishes the charge drained away from C_1 and C_2 during modes 1 and 3. During this period the energy is stored in capacitors C_1 and C_2. The inductor voltage and capacitor current for this mode are given by

$$v_L = V_{in} - \frac{V_o}{2}$$
$$i_C = i_L - \frac{V_o}{2R}. \tag{15}$$

The modes 1 and 3 are separated from each other for one switching period T_s in order to maintain symmetrical waveforms. Actually, for completing all 4 modes, circuit needs two switching periods. Since the C_1 and C_2 are alternately used for discharging the inductor and duration of the modes 2 and 4 is exactly the same, their voltages are theoretically balanced. The voltage transfer ratio is derived combining the equations 10, 14, and 15,

$$M(D) = \frac{2}{1-D}, \tag{16}$$

where D is the duty cycle or duration of modes 1 or 3.

In the second regime ($V_{in} > V_o/2$), the boost inductor charges in modes 1 and 3 (Figure 15), and the output voltage is supplied from the energy stored in the output capacitors. The inductor voltage and capacitor current for this mode are given by

$$v_L = V_{in} - \frac{V_o}{2}$$
$$i_C = i_L - \frac{V_o}{2R}. \tag{17}$$

In modes 2 and 4 the inductor L delivers its stored energy to capacitors C_1 and C_2 via diodes D_1 and D_2, thus charging them up to a higher voltage than V_{in}. This energy supplies the load current and replenishes the charge drained away from C_1 and C_2 during modes 1 and 3. During this period energy is stored in capacitors C_1 and C_2. The inductor voltage and capacitor current for this mode are

$$\begin{aligned} v_L &= V_{in} - V_o \\ i_C &= i_L - \frac{V_o}{R}. \end{aligned} \tag{18}$$

The voltage transfer ratio is derived combining the equations 10, 17, and 18 producing

$$M(D) = \frac{2}{2 - D}. \tag{19}$$

Same as for the first section, the modes 1 and 3 are separated from each other by one switching period T_s, and the duration of modes 2 and 4 is exactly the same.

Since two active switches are used, this converter is more favorable for high power applications. The low device voltage rating benefit is especially important in high voltage applications. Furthermore, this converter greatly decreases the current ripple, which results in using the smaller inductor, thus reducing the cost and size of the converter.

MODE 1

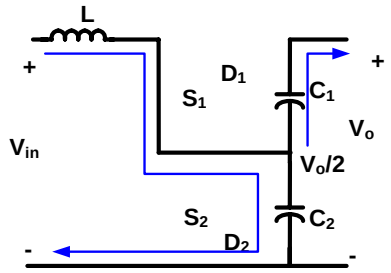

$0 < t < DT_S$

MODE 2

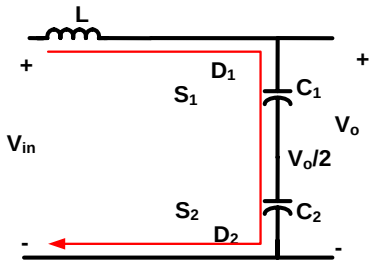

$DT_S < t < T_S$

MODE 3

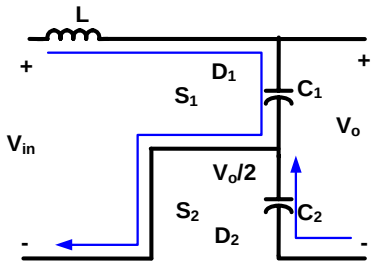

$T_S < t < T_S + DT_S$

MODE 4

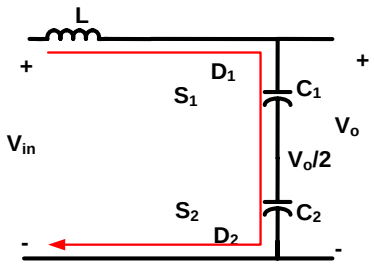

$T_S + DT_S < t < 2T_S$

Fig. 15. Second section operation modes.

3.4 Isolated boost converter

This DC-DC converter topology is an extension of the conventional boost converter. In this case the input and output sides of the converter are isolated by a transformer. The function of the transformer is not only to isolate the grounds of the input and the output but also to provide most of the voltage gain of the converter. The circuit schematic of this converter is shown in Figure 16. The operation principle of this converter is that both switches are kept closed in order to store the energy in the inductors L_1 and L_2; the switches are turned off, one after the other, so the energy is transferred to the load via the

transformer. As can be seen from Figure 16, the converter consists of two switches, two inductors, one transformer, diode-bridge, and output capacitor.

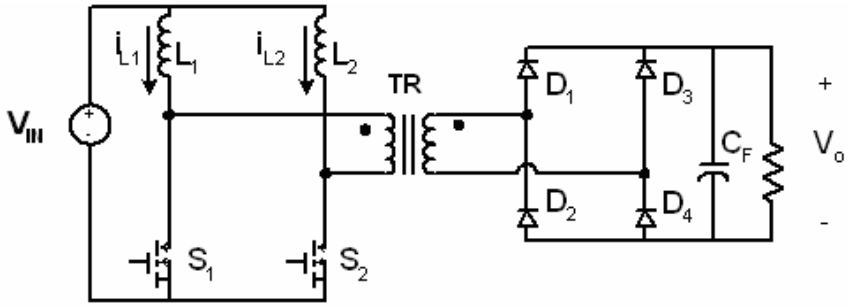

Fig. 16. Conventional two inductor boost converter.

In this case, we have two boost converters connected in parallel. The switches S_1 and S_2 operate alternately in order to invert the input DC voltage to get a square wave at the input terminals of the transformer. This voltage is then stepped up by the transformer and then rectified by the full-wave rectifier at the secondary part of the circuit. Although most of the voltage gain of the converter is due to the transformer, the presence of the input inductors L_1 and L_2 produces a small gain in the same manner as in a boost converter. Voltage conversion ratio is given by

$$M(D) = \frac{n}{1-D}, \tag{20}$$

where *n* is the transformer turn ratio and D is the duty cycle. The duty cycle is defined as a duration of modes 1 or 3 (Figure 17).

These two inductors also allow the converter to work in the continuous conduction mode, which reduces the input current peak value. This makes this converter suitable for high power applications. It is obvious that this topology has a much larger number of components than the previous one, but has the advantage of being suitable for high power applications. In addition, the voltage gain characteristic is better for high gain values than in the case of the boost converter.

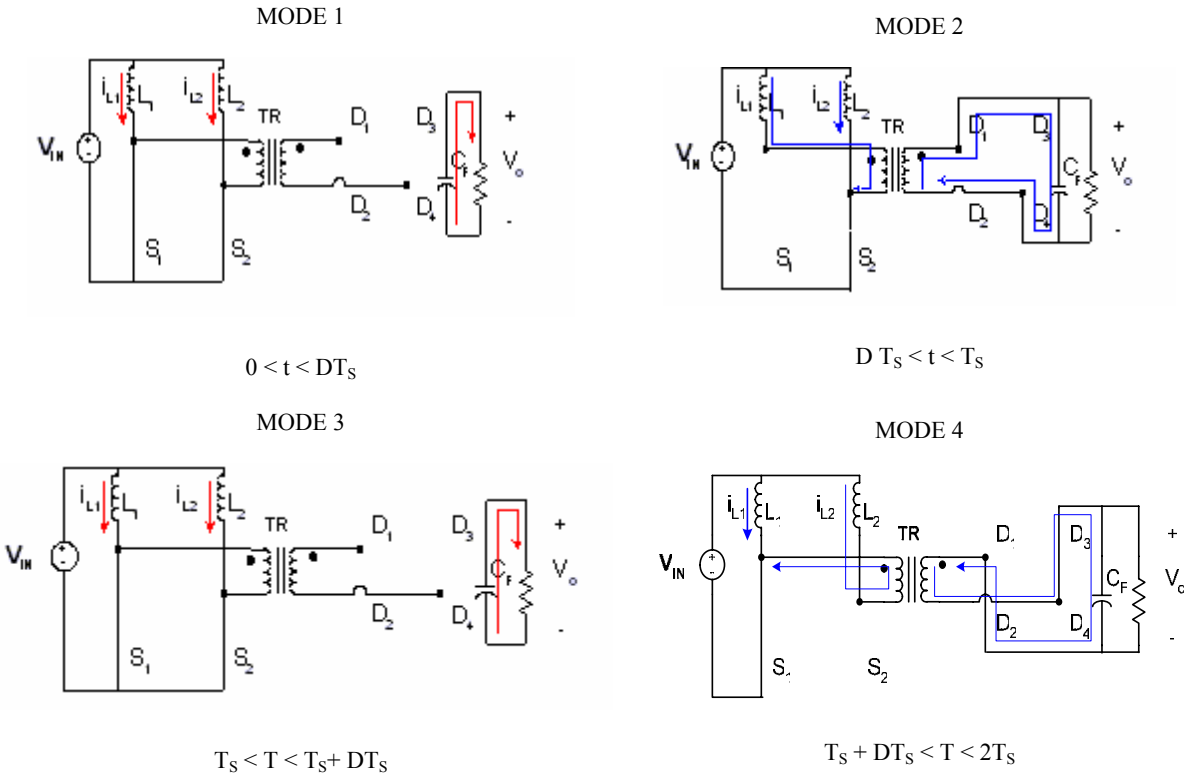

Fig. 17. Two inductor boost operation modes.

The disadvantage of this topology is the high switch stress and its inability to regulate the load in a wide range with constant-frequency control. Solution for this problem would be adding an auxiliary transformer with a unity turns ratio to couple the current paths of the two boost inductors, so that both inductors conduct identical currents. Due to this

current-mirror effect of the auxiliary transformer, no energy is stored in the inductors when there is no overlapping of conduction times of the two switches, i.e., when D=0.

3.5 Push-pull converter

Figure 18 shows the circuit schematic for a push–pull dc-dc converter. This converter is used to produce a square-wave AC signal at the input of the high-frequency transformer. The square wave is then fed to the transformer in order to step-up the voltage. Finally, this voltage is rectified by output diodes to get a DC output.

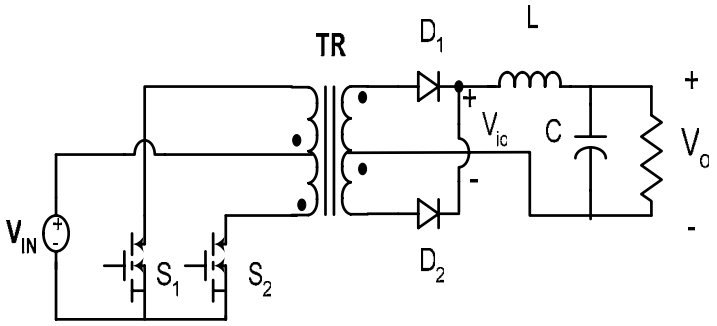

Fig. 18. Push pull converter topology.

Operating modes of a push-pull converter are represented in Figure 19. In the first mode S_1 is on and D_1 conducts; at the same time, the diode D_2 is reverse biased, which produce $V_{io}=nV_{in}$ and voltage across the filter inductor is positive and given as

$$v_L = nV_{in} - V_o, \tag{21}$$

which forces i_L through D_1 to increase linearly. During intervals 2 and 4 (Figure 19) when both switches are off, the inductor current splits equally between the two secondary half-windings and v_{io}=0, which makes

$$\begin{aligned} v_L &= -V_o \\ i_{d1} &= i_{d2} = 0.5 i_L . \end{aligned} \tag{22}$$

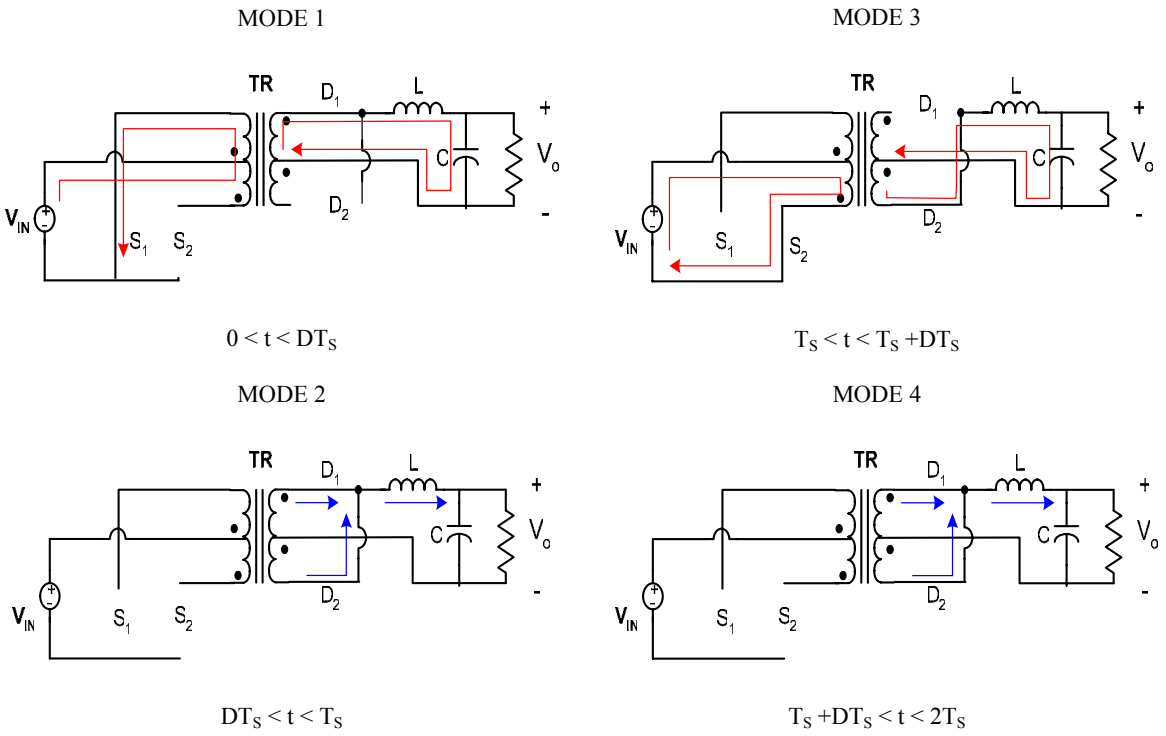

Fig. 19. Push-pull operation modes.

The voltage gain is derived using the previous equations:

$$M(D) = nD , \tag{23}$$

where D is the duty ratio of switches S_1 and S_2 with $0 \leq D < 1$. The ability to operate with the duty cycle approaching unity allows the turn ratio n to be minimized, thus reducing the switches' currents. In practice, this value has to be less than unity to maintain a small blanking time between the two switches since they can not be on at the same time. In this type of converters, due to a slight and unavoidable difference between the switching times of the two switches S_1 and S_2, there is always an imbalance between the peak values of the two switch currents. Also due to its operating characteristic, this converter topology operates in the discontinuous conduction mode, and therefore the switch peak current value tends to be high. The voltage stress to S_1 and S_2 can be two times the input voltage for this kind of converter. This is not extremely high when compared to the other converters discussed in the previous sections. This problem can cause uneven heating of the two switches and produce extra voltage stress on the switch that has to handle a higher current peak value due to the higher di/dt. This problem can be solved by modifying the topology to work in the current mode. This converter topology is discussed in the following point.

3.6 Current-fed push-pull converter

The current-fed push-pull topology is basically the same topology as the voltage-fed topology discussed in the previous subchapter. It only differs in the inductor placed on the input side of the converter as can be seen in Figure 20. By including this inductor in the topology it is possible to operate at duty cycles higher than 100%. When operating at duty cycles higher than 100% the converter operates in the continuous conduction mode reducing the peak value of the switching voltage. This happens because operating at high

duty cycle values implies that the two switches are conducting at the same time for some time periods and therefore the current is not discontinued at any moment.

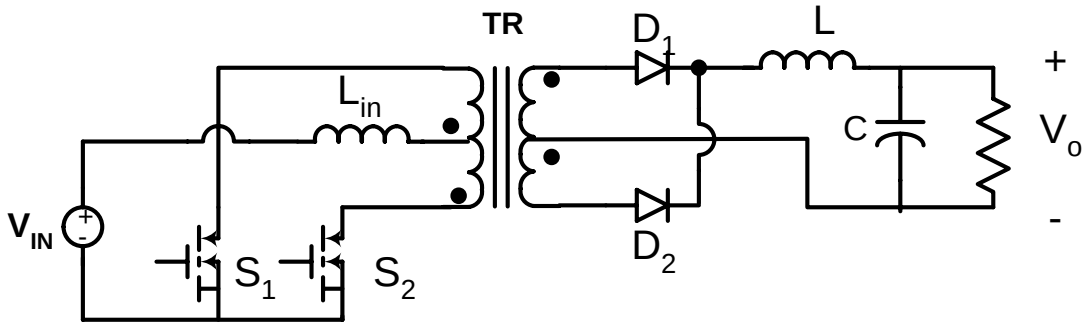

Fig. 20. Current fed push pull converter topology.

When the two switches are on, the voltage on the primary half winding of the transformer becomes zero. The input current builds up linearly and the energy is stored in the input inductor. When only one of the two switches is conducting, the input voltage and the stored energy in the input inductor supply the output stage of the converter. Therefore this converter operates in a manner similar to a boost converter. During the continuous current conduction, i.e. duty cycle bigger than unity, the voltage gain of the converter can be calculated as

$$M(D) = \frac{n}{1-D}. \tag{24}$$

This kind of a converter has the disadvantage of having a low power-to-weight ratio when compared to the converters presented above. Also the voltage stress to the switches is higher than two times the input voltage when the converter is working below unity

duty cycle. Nevertheless, it has the advantage of reducing the peak value of the switch current for high loads because it works in the continuous conduction mode. This makes this DC-DC converter topology a good option for high power applications.

3.7 Full-bridge converter

The full-bridge DC-DC converter is shown in Figure 21, where S_1, S_2 and S_3, S_4 are switched as pairs alternately at the selected switching frequency. When (S_1, S_2) or (S_3, S_4) are on, $v_{io} = nV_{in}$ and therefore $v_L = nV_d - V_o$. During modes 2 and 4 (Figure 22) both pairs of switches are off so the inductor current splits equally between the two secondary halves.

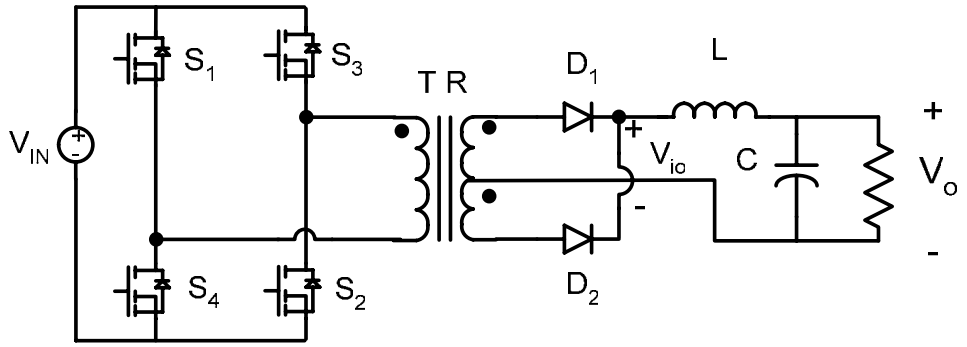

Fig. 21. Full-bridge converter topology.

Assuming the ideal diodes, v_{io}=0, and therefore $v_L = -V_o$. Equating the time integral of the inductor voltage during one repetition period to zero, voltage gain becomes

$$M(D) = nD, \tag{25}$$

where D is the duty cycle. The average of v_{io} equals Vo. The equation (25) is valid for the operation in continuous conduction mode, but this converter can operate in discontinues conduction mode for light loads. The full-bridge converter can operate over essentially whole range of duty cycles. This converter is usually used for high power levels. The utilization of the transformer is good, leading to the small transformer size. In particular, the utilization of the transformer core is very good, since the transformer magnetizing current can be both positive and negative.

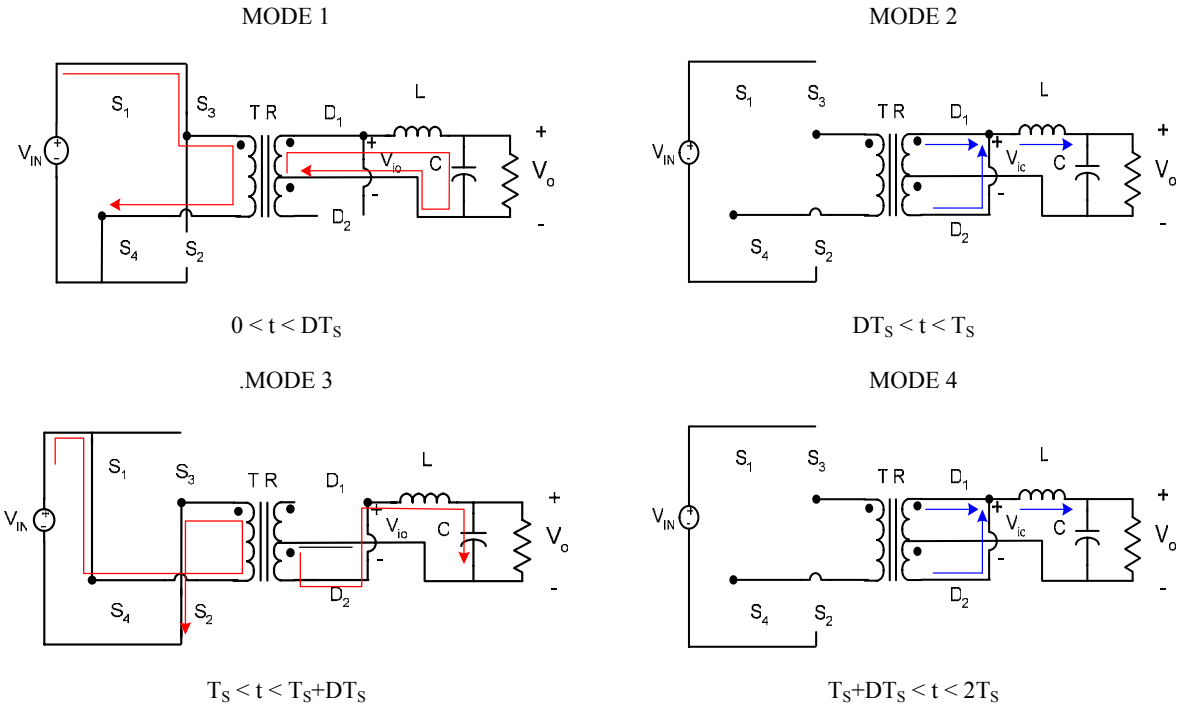

Fig. 22. Full-bridge operation modes.

Hence, the entire B-H loop of the core can be used. The transformer primary winding is effectively utilized, but the center-tapped secondary winding is not, since each half of the center-tapped winding transmits power only during alternate switching periods.

3.8 Half-bridge converter

Figure 23 shows a half-bridge DC-DC converter. The capacitors C_1 and C_2 establish a voltage midpoint between zero and the input voltage. The switches S_1 and S_2 are turned on alternately, each for an interval $t_{on}=DT_s$.

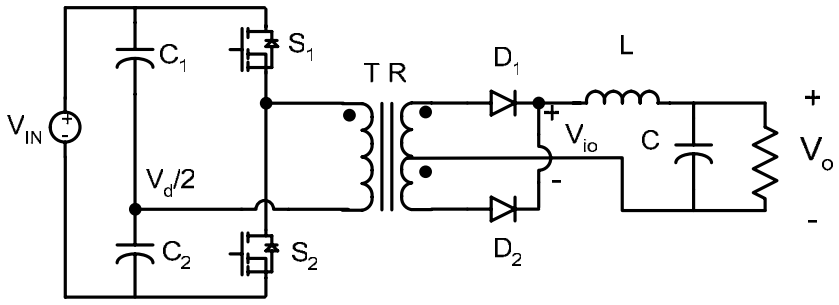

Fig. 23. Half-bridge converter topology.

With S_1 turned on in mode 1 in Figure 24, $v_{io} = n\frac{V_d}{2}$ and therefore $v_L = n\frac{V_d}{2} - V_o$. During modes 2 and 4 (Figure 24), both switches are off so inductor current splits equally between the two secondary halves. Assuming the ideal diodes, $v_{io} = 0$, and therefore $v_L = -V_o$. Equating the time integral of the inductor voltage during one repetition period to zero, voltage gain becomes

$$M(D) = 0.5nD\,. \tag{26}$$

The average of v_{io} equals Vo. The diodes in antiparallel with the switches S1 and S2 are used for switching protection, as in a push-pull converter. From equation (26) we can

conclude that the output voltage of the half bridge is reduced by a factor of 2 comparing with the full-bridge converter. This factor can be compensated for by doubling the transformer ratio n. However, this causes the transistor current to double.

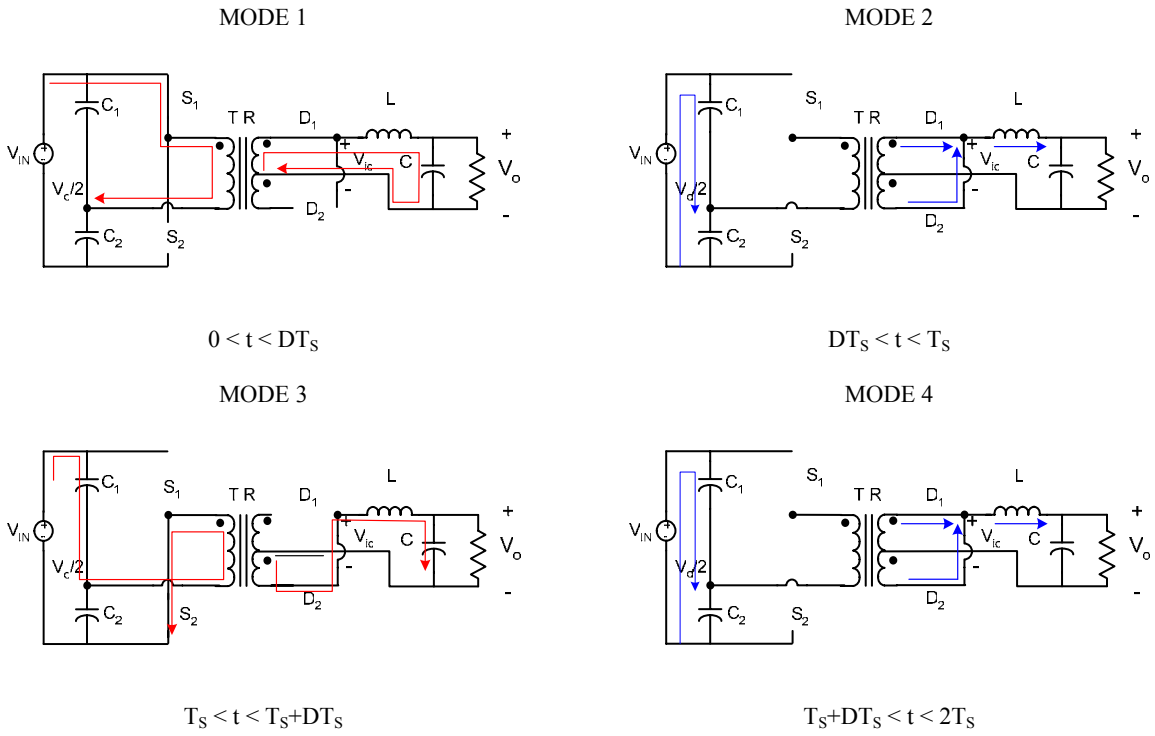

Fig. 24. Half-bridge operation modes.

Hence, the half-bridge configuration needs only two switches rather than four, but these two switches must handle currents that are twice as large as those of the full-bridge circuit. In consequence, half-bridge configuration finds applications at lower power levels. Utilization of the transformer core and windings is essentially the same as in the full-bridge configuration.

3.9 Forward converter

An idealized forward converter is shown in Figure 25. In this type of the converter magnetizing current must be taken into account. Initially, if we assume that the transformer is ideal, when the switch is on, diode D_1 becomes forward biased and D_2 reverse biased. Voltage across the inductor is $v_L = nV_d - V_o$, which is positive and i_L is increasing. When the switch is turned off, the inductor current circulates through the diode D_2, and $v_L = -V_o$, which is negative and therefore causes i_L to decrease linearly. Equating the time integral of the inductor voltage during one repetition period to zero, voltage gain becomes

$$M(D) = nD\,. \tag{27}$$

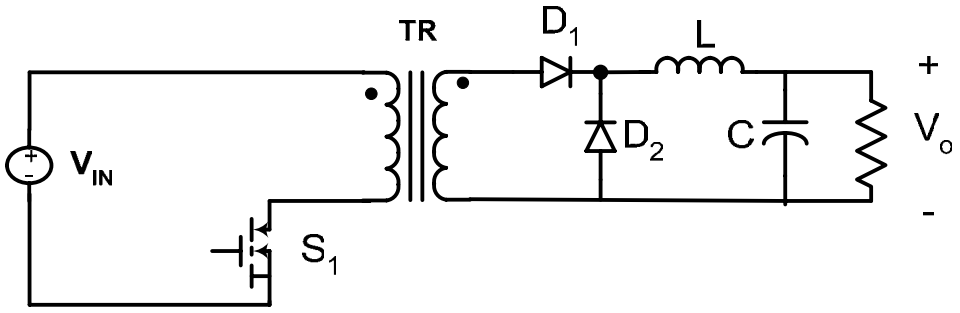

Fig. 25. Forward converter topology.

In a practical converter, the transformer magnetizing current must be taken into consideration for proper operation. Without that, the stored energy in the transformer core would result in the converter failure. An approach that allows the transformer magnetic energy to be recovered and fed back to the input supply is shown in Figure 26.a.

When the switch is on, $v_1 = V_{in}$ for 0<t<t_{on} and i_m increases linearly from zero to I_m. When the switch is turned off $i_1 = -i_m$, with directions shown in Figure 26.b. Current directions in Figure 26.b make the continuity of the flux expressed as $N_1 i_1 + N_3 i_3 = N_2 i_2$. Because of diode D1, i_2=0 and $i_3 = \frac{N_1}{N_3} V_{in}$, which flows through D_3 into the dc supply. The voltage on the primary side is $v_1 = -\frac{N_1}{N_3} V_{in}$ for t_{on} <t<t_{on}+t_m. Once the transformer demagnetizes, i_m=0 and v_1=0. Equating the time integral of the voltage v_1 to zero yields $t_m = \frac{N_3}{N_1} DT_s$. If the transformer is to be totally demagnetized before the next cycle begins, the maximum value t_m/T_s can attain 1-D. Therefore the maximum duty ratio D_{max} is given by

$$D_{\max} = \frac{1}{1 + N_3 / N_1}. \tag{28}$$

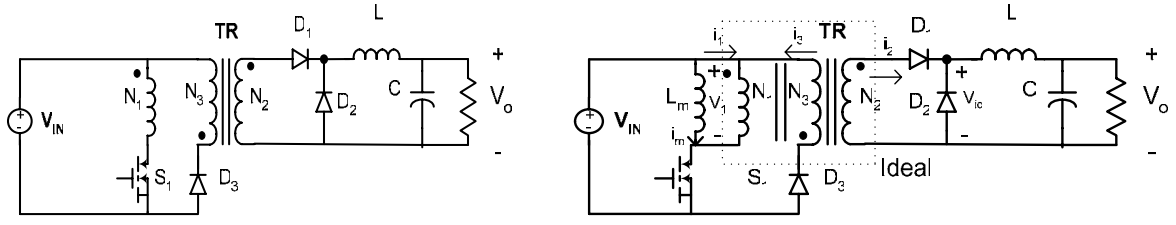

a) b)

Fig. 26. a) Practical forward converter topology and b) Equivalent circuit.

The above analysis shows that with the equal number of turns for the primary and the demagnetizing windings (N_1=N_3), the maximum duty ratio in such converter is limited to 0.5. Voltage gain remains the same as for the ideal transformer case.

The utilization of the transformer of the forward converter is quite good. Since the transformer magnetizing current cannot be negative, only half of the core B-H loop can be used. This would imply that the transformer should be twice as large as those of full-bridge or half-bridge converters. However, in high-frequency converters the flux is constrained by core losses rather than the core saturation flux density. Utilization of the primary and secondary windings of the transformer is better than in the full-bridge, half-bridge or push-pull configurations, since the forward converter requires no center-tapped windings. Typically, the magnetizing current is small compared to the reflected load current, so it has a negligible effect on the transformer utilization.

3.10 Flyback converter

Flyback converter is shown in Figure 27. When the switch S_1 is conducting, the energy from the DC source V_{in} is stored in L_m. When the diode D_1 conducts, this stored energy is transferred to the load, with the inductor's voltage and current scaled according to the 1:n turns ratio. During the first subinterval $v_L = V_{in}$, while during the second subinterval $v_L = -\frac{V_o}{n}$. Equating the time integral of the inductor voltage during one repetition period to zero, voltage gain becomes

$$M(D) = n\frac{D}{1-D} \tag{29}$$

The flyback converter is commonly used in the 50 to 100 W power range. It has the advantage of a very low parts count. Multiple outputs can be obtained with just adding one winding, diode and capacitor.

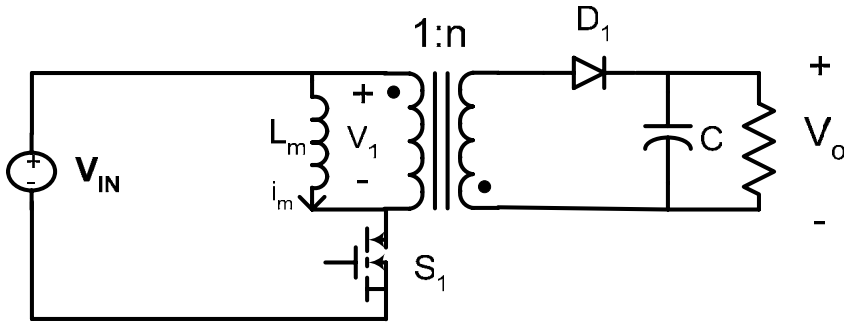

Fig. 27. Forward converter topology.

However, in comparison with the full-bridge, half-bridge or forward converters, the flyback has the disadvantage of high transistor voltage stress and poor cross-regulation. The peak switch voltage is equal to input voltage plus the reflected load voltage *Vo/n*; in practice additional voltage due to ringing is observed. The magnetizing current of the flyback converter is unipolar, thus no more than half of the core material B-H loop can be utilized and also it contains a significant DC component. Yet, the size of the flyback transformer is quite small in designs intended to operate in discontinuous conduction mode. This leads to increased peak currents in the switch, diode and capacitor

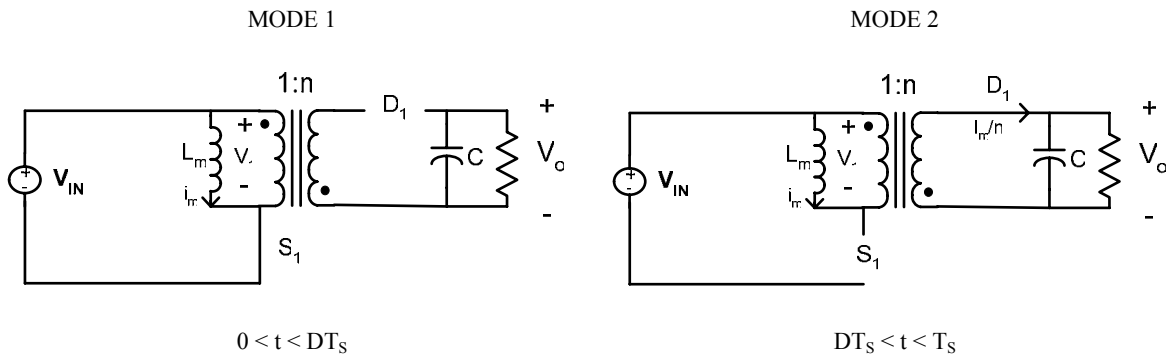

Fig. 28. Flyback operation modes.

3.11 Comparison between topologies

Often, the largest cost in a converter is the cost of the semiconductor devices. Also, the conduction and switching losses associated with the semiconductor devices often dominate the total converter losses. Thereby evaluating semiconductor switch utilization is a good tool to compare different converter topologies. It is useful to compare the total active stress and active switch utilization of different converter topologies. If a converter topology contains *k* active semiconductor devices, the total switch stress S can be defined as

$$S = \sum_{j=1}^{k} V_j I_j \ , \tag{30}$$

where *Vj* is the peak voltage applied to the *j*-th semiconductor device, and I_j is the rms current applied to the *j*-th switch [20].

Table III Switch utilization comparison

Converter	U(D)	max U(D)	max U(D) occurs at D=
Boost	$\frac{1-D}{\sqrt{D}}$	∞	0
Three-level boost	$\frac{2-D}{\sqrt{2D}}$	∞	0
Isolated boost	$\frac{1-D}{\sqrt{2-D}}$	$\frac{1}{\sqrt{2}}$=0.7071	0
Push-pull	$\frac{\sqrt{D}}{2\sqrt{2}}$	$\frac{1}{2\sqrt{2}}=0.353$	1
Current fed push-pull	$\frac{1-D}{2\sqrt{1+D}}$	0.5	0
Full-bridge	$\frac{\sqrt{D}}{2\sqrt{2}}$	$\frac{1}{2\sqrt{2}}=0.353$	1
Half-bridge	$\frac{\sqrt{D}}{2\sqrt{2}}$	$\frac{1}{2\sqrt{2}}=0.353$	1
Forward, N_1=N_2	$\frac{1}{2}\sqrt{D}$	$\frac{1}{2\sqrt{2}}=0.353$	$\frac{1}{2}$
Flyback	$(1-D)\sqrt{D}$	$\frac{2}{3\sqrt{3}}=0.385$	$\frac{1}{3}$

If the converter output power is P_{Load}, then the active switch utilization U can be defined as

$$U = \frac{P_{Load}}{S}. \tag{31}$$

The switch utilization is less than one for transformer isolated converters, and is a quantity depending on the duty cycle. A comparison between the converter topologies discussed in previous points is shown in Table III above.

From Table III it can be seen that the boost and three-level boost converters switch utilization is greater than one for duty cycles bigger than 0.382, and approaches infinity as D approaches zero. The reason for this is that, at D=0, the switch is always in its OFF state and its rms current is zero. But at D=0 the output voltage is equal to the input voltage and the converter output power is nonzero.

Also from Table III it is possible to see that the incorporation of an isolation transformer results in a reduced switch utilization. Therefore this type of converters should be designed to operate preferably at a duty cycle as high as possible. Finally from the previous table it is possible to see that the flyback topology has lower switch utilization than the boost converter.

3.12 Conclusion

There is no ultimate converter perfectly suited for all applications. For a given application, with given specifications, trade off studies should be performed to select the converter topology. Several approaches that meet the specifications should be considered, and for each approach important quantities such as worst case semiconductor device rms current, size, component count, etc. should be computed. This type of quantitative comparison can lead to selection of the best approach.

CHAPTER IV
WIDE INPUT RANGE DC-DC CONVERTER DESIGN

4.1 Introduction

Since the DC voltage generated by a fuel cell stack varies widely and is low in magnitude (<60 V for a 5-10 kW system, <350 V for a 300 kW system), a step-up DC-DC conversion stage is essential to generating a higher regulated DC voltage (400 V typical for 120/240 V AC output). Due to the nature of the fuel supply process, the cell response time to changes in power demand is high and varies from few seconds to a minute [21,22]. Therefore, it is necessary to improve the dynamics of the system by introducing auxiliary devices. Those auxiliary devices could be ultracapacitors or batteries and both are used in this thesis. There are several proposed solutions using bidirectional DC-DC converters for charging/discharging the auxiliary battery packs or other energy storage devices [23, 24], but this results in additional costs and converter volume. Following these stages a DC-AC inverter is used to supply the ac voltage to the load.

The following subchapters present a novel DC-DC converter configuration that improves the utilization of the high-frequency transformer in the step-up stage and simplifies the control of the whole system. This configuration uses fewer components and is more cost-efficient than the previously proposed solutions.

4.2 System design

Figure 29 shows a block diagram of the 5 kW fuel cell power conditioner. The DC voltage input varies in a wide range from 36 V to 60 V and the output AC voltage is maintained at 120/240 V.

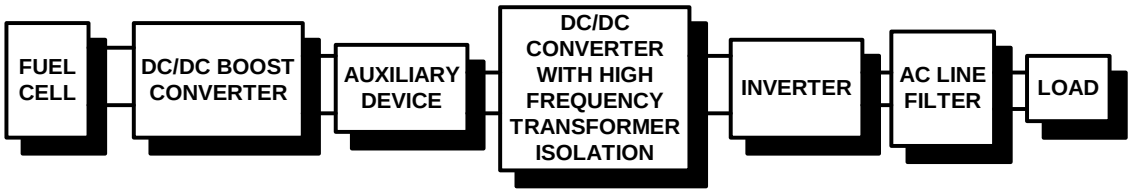

Fig. 29. Block diagram of the complete system.

The input DC voltage from the fuel cell is first stepped up to a regulated 80 V using a high frequency parallel three-level boost converter. The 80 V DC-DC converter output is then converted to 400 V by means of a DC-DC converter with high frequency isolation. This voltage is finally inverted using a PWM driven inverter stage to supply a 120/240 V, 50/60 Hz, bi-phase AC voltage. An output LC filter stage is employed to produce a low THD AC waveform. An ultracapacitor or a battery is floated in the 80V DC bus to supply energy during sudden load demands.

The efficiency of the high-frequency transformer in the DC-DC converter stage depends on the stability of the input voltage. The transformer needs to be designed to accommodate the lowest voltage levels. During the normal operation the nominal input voltages are typically much higher than the minimum value and the transformer does not operate optimally. The fuel cell power conditioner presented in this thesis overcomes this by regulating the input voltage of the second stage at 80 V. Therefore, the isolated DC-

DC converter can operate in open loop, thus simplifying the control of the entire system. Additionally, since the input voltage of the isolated DC-DC converter is higher, the current ratings of the switches can be much lower, which, together with the lower transformer ratio, reduces the overall cost of the system.

4.3 Proposed DC-DC converter topology

Since the fuel cell terminal voltage varies significantly depending on the load current that it is supplying, a wide input range DC-DC converter is required to boost and regulate the fuel cell voltage. Other key requirements for DC-DC converters for this type of applications are high efficiency and galvanic isolation. As shown in the block diagram of Figure 29 this converter has two boosting stages connected in series. The critical issue in the design of the fuel cell conditioner is the first stage DC-DC converter because the optimal performance of the second stage depends on the proper operation of the first stage. Additional requirement is the strict control of the auxiliary device, which enhances the dynamics of the fuel cell powered system. All that being said, this thesis focuses on the design and control of the primary boost converter in the first stage of the conditioner and on the proper control of the auxiliary ultracapacitors or batteries. The second stage boost converter can be any of the converters presented in Chapter III that has a high-frequency transformer such as the isolated boost converter.

Figure 30 shows a more detailed schematic diagram of the primary three-level parallel boost converter configuration that steps the voltage up to 80 V. This configuration was chosen instead of the conventional boost converter because of the smaller size of the inductor needed to achieve comparably low ripple [23] as mentioned

in Chapter III. This configuration of the converter also reduces the required semiconductor device voltage rating by a factor of two.

Furthermore, having two identical three-level boost converters in parallel decreases the current ratings of used semiconductor devices, decreases conduction losses, and increases overall efficiency. This will be elaborated upon in the following section.

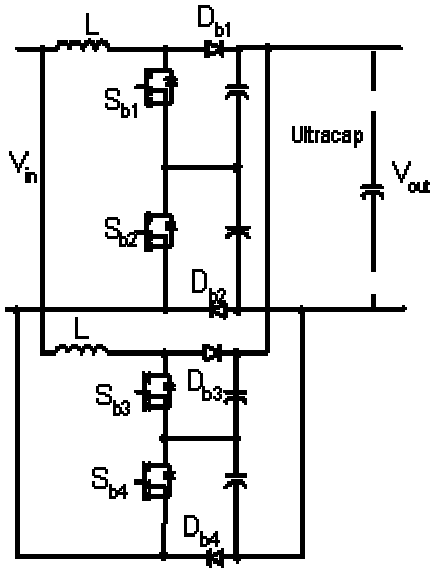

Fig. 30. Proposed DC-DC converter topology suitable for wide input voltage range.

Three-level boost converter can operate in two different modes depending on whether the input level is lower or higher than half of the output voltage V_o [23]. These modes were explained in detail in Chapter III. In this particular application the input voltage is always higher than half of the output voltage because when the maximum power is delivered the input voltage is equal to its nominal value of 42V. It can be shown that the boost inductor charging voltage is V_{in}-$V_o/2$ and the discharging voltage is defined by V_o-V_{in}, which results in the current waveforms shown in Figure 31. In this figure S_{b1} and S_{b2} are the gating signals for the switches having a duty cycle (D) smaller than 50%.

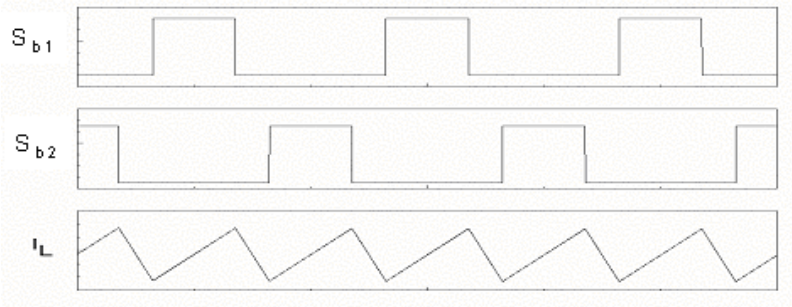

Fig. 31. Operation waveforms for first stage DC-DC converter.

In this mode of operation ($V_{in}>V_o/2$) the current ripple is maximum for D=0.5, which corresponds to the a input voltage of $V_{in}=0.75V_o$. The maximum current ripple is given by

$$\Delta i \max = \frac{V_{in} - 0.5V_o}{L} \frac{DT_S}{2} = \frac{V_o T_s}{16L} \tag{32}$$

which corresponds to one fourth of the maximum current ripple in a conventional boost configuration.

4.4 Selection of the first boosting stage

In order to justify the selection of the parallel three-level boost converter for the primary boosting stage of the fuel cell conditioner, a comparison of three configurations, of which none has the transformer in its topology, is presented. The configurations being compared are the parallel three-level boost (#1), the three-level boost (#2) and the conventional boost (#3) converter.

The efficiency, conduction and switching losses for the same power level of 5 kW (1 pu), as well as the number of components for these configurations are shown in Table IV.

Table IV Efficiency and power losses comparison

	#1	#2	#3
Number of components	4D+4SW	2D+2SW	3D+3SW
Inductor current [pu]	0.5	1	1
SW conduction losses [pu]	10.16*E-3	15.14*E-3	10.95*E-3
Diode conduction losses [pu]	25.71*E-3	41.61*E-3	15.91*E-3
Switching losses [pu]	21.07*E-3	43.59*E-3	15.94*E-3
Efficiency	94.31%	89.97%	95.72%

The switching (SW) conduction losses represent conduction losses in the converter's MOSFETs and they can be calculated using equation 33

$$P_{SW} = \frac{1}{T}\int V_{DS} I_S \tag{33}$$

where V_{DS} is a drain-source voltage across the switch while it conducts, and I_S is the current through the switch.

Diode conduction losses can be calculated using

$$P_{DIODE} = \frac{1}{T}\int V_F I_F \tag{34}$$

where V_F is a forward voltage drop and I_F is a diode forward current of a diode. The values of V_F and V_{DS} can be obtained from manufacturer's data sheets and they depend on the current through the device.

Switching losses consist of turn-on and turn-off losses in the MOSFET as shown in equations. 35 and 36, respectively, while reverse recovery losses in the diode are considered approximately zero.

$$P_{ON} = \frac{1}{T}[0.5 I_S \Delta V_{DS} (t_{on} + t_r)] \tag{35}$$

$$P_{OFF} = \frac{1}{T}[0.5 I_S \Delta V_{DS} (t_{off} + t_f)] \tag{36}$$

Times t_{off}, t_{on}, t_r, and t_f can be obtained from the data sheets and represent the turn-off, turn-on, rising and falling times, respectively.

As can be seen from Table 4, second configuration is clearly inferior to the other two regarding the power losses and efficiency. The conventional boost and the parallel three-level boost converters have comparable efficiencies and similar number of components. However, the voltage and current ratings of switches and diodes used in the conventional boost converter have to be twice as big as the ratings of components in configuration #1 [23], thus increasing size and cost. In addition, the inductor in #3 has to be larger than the others to achieve the same current ripple levels. Therefore, the best choice for the power conditioner is to use the parallel three-level configuration.

Additional improvements regarding power losses can be made using the synchronous rectifiers instead of diodes [24]. The power losses in diodes are usually much greater than

losses in the channel of a field effect device, which reduces the efficiency of the converter. Although this configuration reduces losses, it is not being implemented at this stage due to the complexity of finding the optimum on and off times for the rectifier switches.

4.5 Secondary DC-DC converter

The second stage, composed of an isolated two inductor boost converter, boosts the voltage to its final level. This two inductor boost converter shown in Figure 32 was derived from the Weinberg boost converter [25], and has as advantages a high efficiency (above 90% for full load) and improved output voltage regulation.

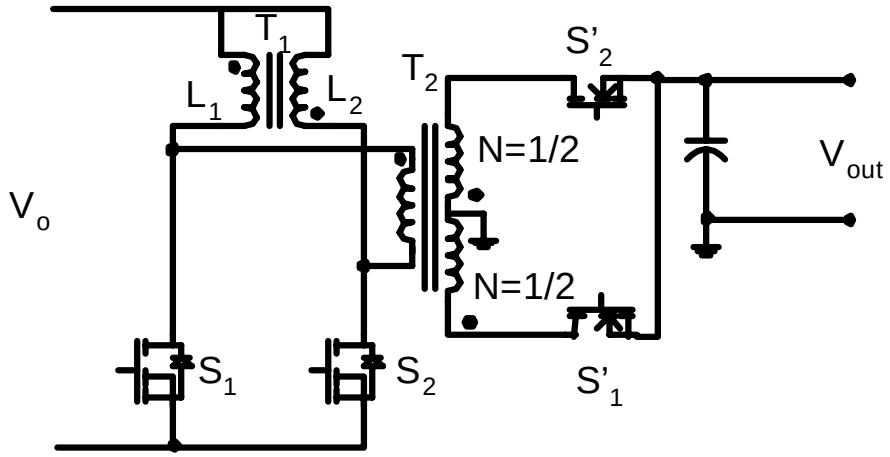

Fig. 32. Proposed secondary DC-DC converter topology.

It uses two coupled inductors L_1 and L_2, and the alternating operation of switches S_1 and S_2 to get a primary voltage gain. The galvanic isolation between the input and output of the converter, along with additional boosting, is provided by the transformer T_2.

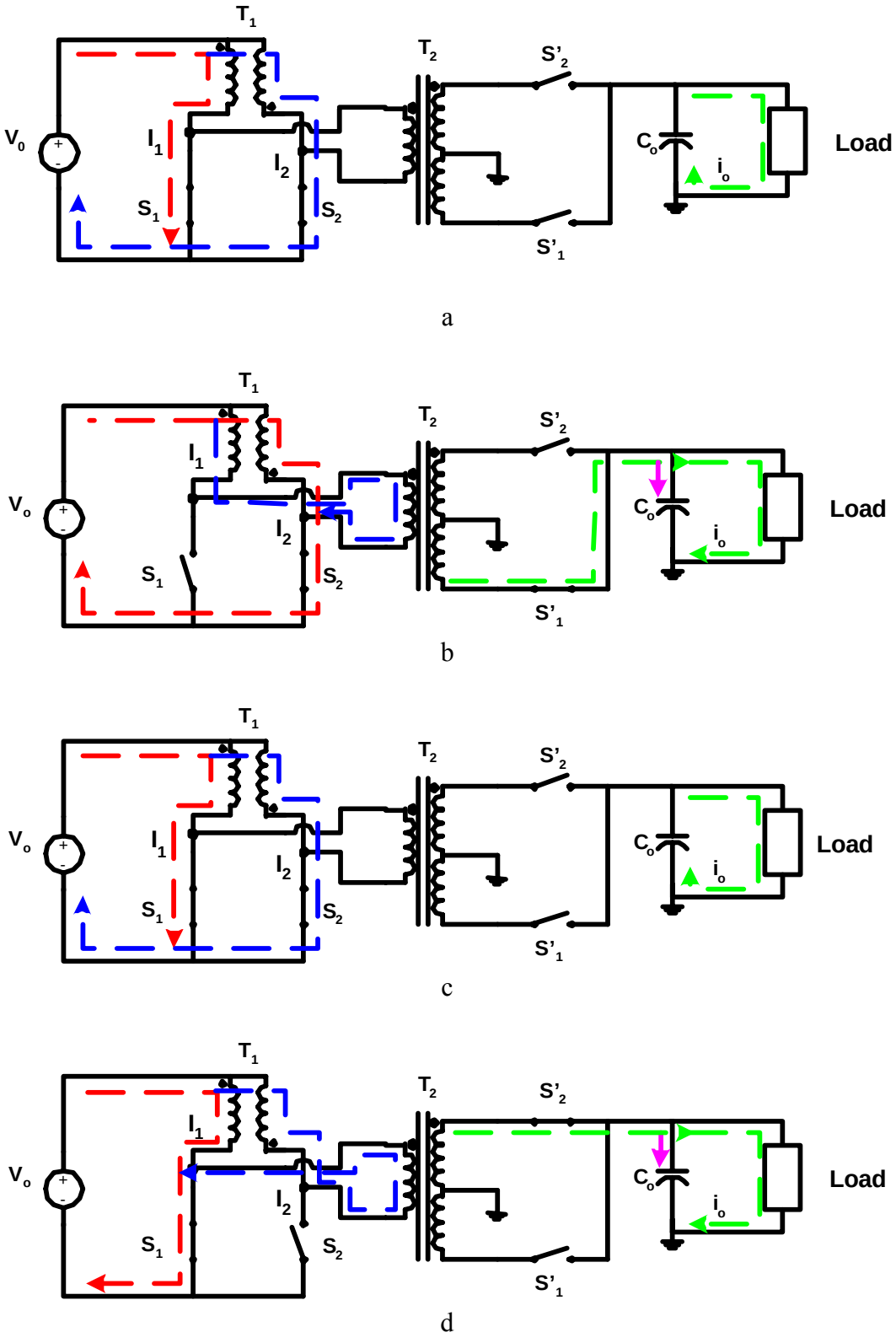

Fig. 33. Operating states of the secondary boosting stage.

The voltage gain of the converter is obtained from

$$\frac{V_{out}}{V_o} = \frac{n_2}{n_1}\frac{2}{1-D} \tag{37}$$

where n_1 and n_2 are the primary and secondary turn's ratio of the transformer T_2, and D is the converter's duty cycle.

A synchronous rectifier is used on the secondary side of the converter to rectify the voltage and increase the efficiency of the converter. The gating signals for the output rectifier switches S'_1 and S'_2, are synchronized with their primary counterparts S_1 and S_2 respectively. The operation of the converter can be broken down in 4 states shown in Figure 33. The first stage is shown in Figure 33a; here the two primary switches S_1 and S_2 are closed and the rectifier switches S'_1 and S'_2 are maintained open. In this case the currents I_1 and I_2 through inductors L_1 and L_2 build up and the load is being supplied by the energy stored in the output capacitor. In the second state switch S_1 is opened and switch S_2 is kept closed, which allows the inductors L_1 and L_2 to supply energy to the primary side of the transformer T_2. During this state the voltage across the lower transformer secondary winding is positive with respect to ground so switch S'_1 is closed to supply the load and the output capacitor. During the third converter state shown in Figure 33c, S_1 is closed again to allow the inductor's current to build up and the load is supplied by the output capacitor in the same fashion as during the first state. During the fourth converter state (Figure 33d) switch S_2 is opened while S_1 is kept closed allowing current to flow in the opposite direction as in the second state. This has the effect of

producing a positive voltage across the top secondary winding, thus S'_2 is closed while S'_1 is kept open to supply the load and the output capacitor.

Figures 34 and 35 show the timing diagram for the converter operation. The waveforms correspond to the converter supplying a 5 kW load with an 80 V input voltage.

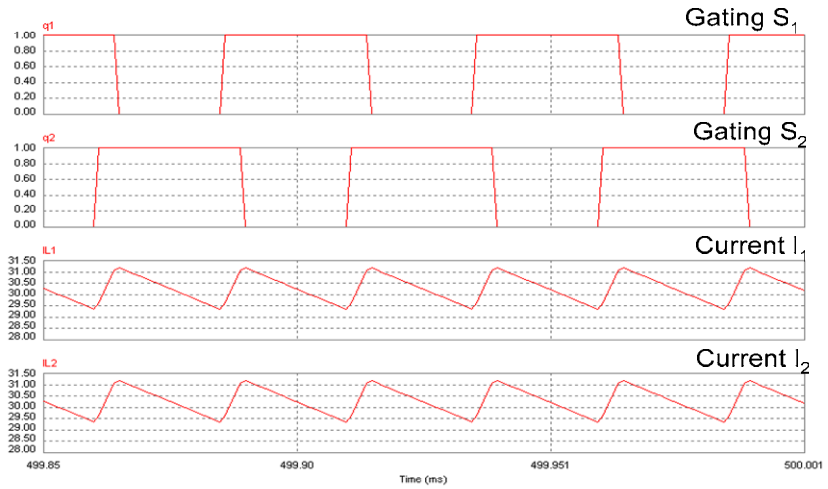

Fig. 34. Timing diagrams for second stage DC-DC converter – primary side of T2.

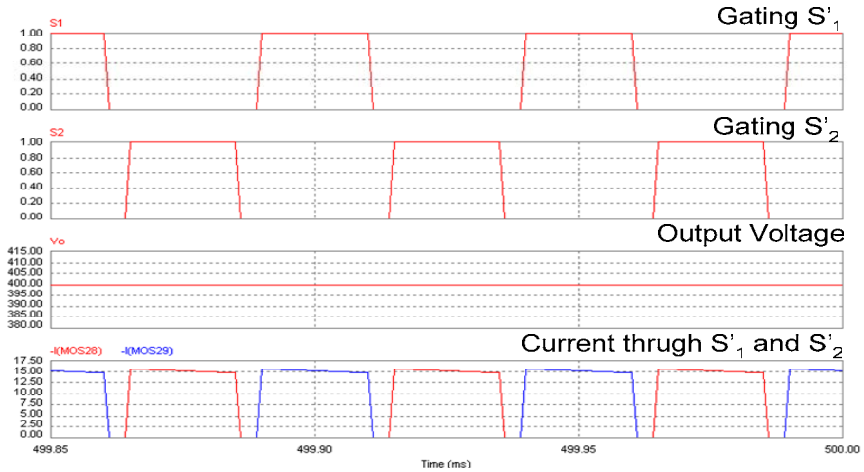

Fig. 35. Timing diagrams for second stage DC-DC converter – secondary side of T_2.

4.6 Control design

Converter systems regularly require feedback. For example, in a typical DC-DC application, the output voltage must be kept constant, regardless of changes in the input voltage or in the effective load resistance. This is accomplished by building a circuit that varies the converter's control input (i.e. the duty cycle D) in such a way that the output voltage is regulated to be equal to the desired reference value. To design the control system, we need a dynamic model of the switching converter. We will observe the output voltage as a function of the input voltage, the load current and the duty cycle. The resulting AC equivalent circuits will be similar to the DC equivalent circuits derived in Chapter III.

The analysis will begin by determining the voltage and current of the inductor and capacitors. The operating modes are given in Figure 15 and inductor voltages and capacitor currents in these modes are:

Mode 1:

$$\begin{aligned} v_L &= v_{IN} - v_O / 2 \\ i_{C1} &= -\frac{v_O}{R} \\ i_{C2} &= i_G - \frac{v_O}{R} \end{aligned} \tag{38}$$

Mode 2:

$$\begin{aligned} v_L &= v_{IN} - v_O \\ i_{C1} &= -\frac{v_O}{R} + i_G \\ i_{C2} &= -\frac{v_O}{R} + i_G \end{aligned} \tag{39}$$

Mode 3:

$$\begin{aligned} v_L &= v_{IN} - v_O / 2 \\ i_{C1} &= -\frac{v_O}{R} + i_G \\ i_{C2} &= -\frac{v_O}{R} \end{aligned} \tag{40}$$

Mode 4:

$$\begin{aligned} v_L &= v_{IN} - v_O \\ i_{C1} &= -\frac{v_O}{R} + i_G \\ i_{C2} &= -\frac{v_O}{R} + i_G \end{aligned} \tag{41}$$

where all these signals represent sums of DC and AC signals. By averaging the above waveforms over one switching period and eliminating the nonlinear second order AC terms we get the operational equations describing the DC and AC equivalent circuits.

Averaging the inductor voltage v_L will produce the DC term:

$$V_O = \frac{2}{2-D} V_{IN} \tag{42}$$

and the AC term:

$$v_l = v_{in} + V_O \frac{d}{2} - v_o \frac{2-D}{2}. \tag{43}$$

Similarly, averaging the capacitors' currents i_{C1} and i_{C2} will produce the DC term:

$$I_{IN} = \frac{2}{2-D}\frac{V_O}{R} \tag{44}$$

and the AC term:

$$i_{c1} = i_{c2} = -\frac{v_o}{R} - I_{IN}\frac{d}{2} + i_{in}\frac{2-D}{2}. \tag{45}$$

This leads to AC equivalent circuits shown in Figure 36 representing the inductor loop equation as well as capacitor node equations.

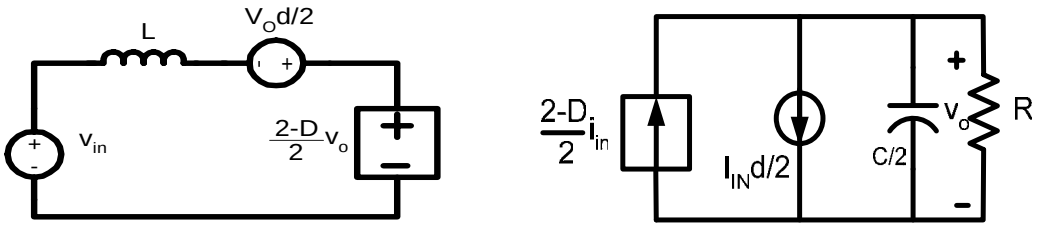

Inductor loop Capacitor current

Fig. 36. Three-level boost AC equivalent circuits.

These three equations could be collected in one AC equivalent circuit equation by combining the dependent sources into the ideal transformer with transfer ratio of M(D)=$\frac{2-D}{2}$, leading to the final model.

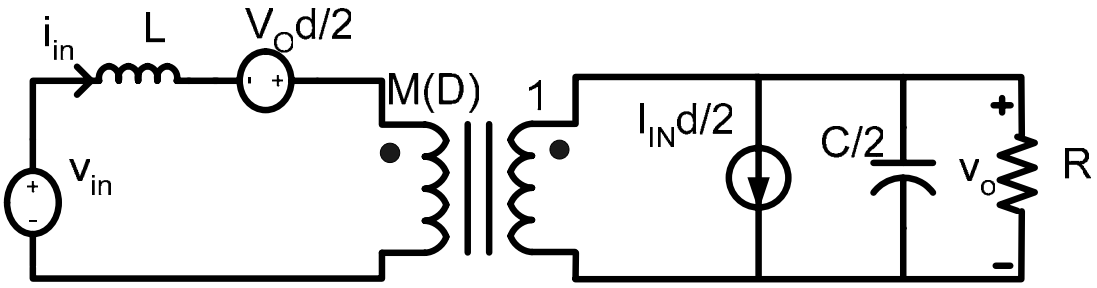

Fig. 37. Three-level boost AC equivalent model.

There are different transfer characteristic that we can derive from model in Figure 37. The line-to-output transfer function $G_{vi}(s)$ is found by setting duty cycle variation d(s) to zero, and then solving for the transfer function from $v_{in}(s)$ to $v_o(s)$.

$$G_{vi} = \left.\frac{v_o(s)}{v_{in}(s)}\right|_{d(s)=0} \tag{46}$$

This transfer function describes how variations or disturbances in the applied input voltage $v_{in}(t)$ lead to disturbances in the output voltage $v_o(t)$ and it is important for designing the output voltage regulator.

The control-to-output transfer function $G_{vd}(s)$ is found by setting the input voltage variation $v_{in}(s)$ to zero, and then solving the equivalent model for $v_o(s)$ as a function of d(s).

$$G_{vd} = \left.\frac{v_o(s)}{d(s)}\right|_{v_{in}(s)=0} \tag{47}$$

This transfer function describes how the control input variations d(s) influence the output voltage $v_o(s)$. In an output voltage-regulated system, $G_{vd}(s)$ is a key component of the loop gain and has a significant effect on the performance of the regulator.

The output impedance $Z_{out}(s)$ is found under the conditions that $v_{in}(s)$ and d(s) variations are set to zero. $Z_{out}(s)$ describes how variations in the load current affect the output voltage. It is appropriate to define $Z_{out}(s)$ either including or not including the load resistance R.

$$Z_{out} = -\left.\frac{v_o(s)}{i_{load}(s)}\right|_{\substack{v_{in}(s)=0 \\ d(s)=0}} \tag{48}$$

To derive the control-to-output and line-to-output transfer functions we will use the small-signal equivalent model shown in Figure 37 as well as equations 46 and 47. Line-to-output transfer function is given by:

$$G_{vi}(s) = G_{i0}\frac{1}{1+\frac{s}{Q\omega_o}+\left(\frac{s}{\omega_o}\right)^2}$$

where (49)

$$G_{io} = \frac{2}{2-D};\ \omega_o = \frac{2-D}{\sqrt{2LC}};\ Q = (2-D)\frac{R}{4}\sqrt{\frac{2C}{L}}.$$

Similarly the control-to-output transfer function is given by:

$$G_{vd}(s) = G_{d0}\frac{1-\frac{s}{\omega_z}}{1+\frac{s}{Q\omega_o}+\left(\frac{s}{\omega_o}\right)^2}$$

where (50)

$$G_{do}=\frac{V_o}{2-D};\ \omega_z=\frac{(2-D)V_o}{2LI_{in}};\omega_o=\frac{2-D}{\sqrt{2LC}};Q=(2-D)\frac{R}{4}\sqrt{\frac{2C}{L}},$$

and the output impedance is given by:

$$Z_{out}=\frac{4Ls}{(2-D)^2+s^2 2LC}. \quad (51)$$

Fuel cells practically have linear voltage-current characteristic as shown in Figure 2 (see page 8), which allows easy calculation of the cell's output power. This relationship is used to calculate the current-limit setting of the DC-DC converter using the Power Available (PA) signal (analog) provided by the fuel cell. This ensures that the power drawn from the fuel cell does not exceed the cell's capability at any given moment. The remaining power necessary to satisfy the load is provided by the energy stored in the ultracapacitor or battery (Figure 29). The inverter, on the other hand, determines the actual power drawn by the load and communicates that information to the fuel cell to either increase or decrease its power output. This ensures that the fuel cell has sufficient time to adjust its power generation to meet the changes in load demand.

The control diagram for the three-level boost converter is illustrated in Figure 38. The inner PI control loop controls the current drawn from the fuel cell and the outer voltage

PI control is used to regulate the output voltage delivered to the ultracapacitor or battery to its reference value.

Three different scenarios are possible when the fuel cell system supplies the load. First situation occurs when the fuel cell system is capable of fully supplying the load demand and the boost converter maintains the constant ultracapacitor or battery voltage. In the second scenario, the fuel cell system is unable to accommodate the load, so the auxiliary device (ultracapacitor or battery) feeds one part of the load thus decreasing its charge. The last possibility refers to a situation when the fuel cell must supply not only the load but also charge the ultracapacitor or the battery.

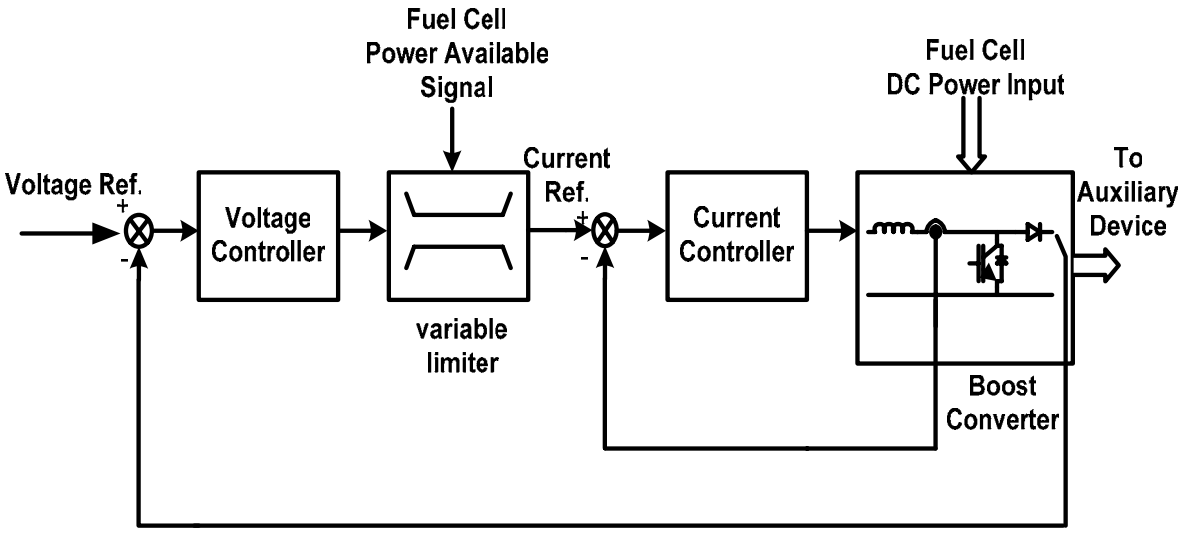

Fig. 38. Block diagram of the boost converter control subsystem.

Using the control diagram from Figure 38 and the averaged small-signal converter models derived earlier, we can find the effects of feedback on the small-signal transfer function. The more detailed block diagram is shown in Figure 39. The output voltage is measured using the voltage sensor with a gain $H_v(s)$ and the inductor's current is

measured using the current sensor with gain $H_i(s)$. The voltage sensor output is compared with the reference input voltage $v_{ref}(s)$. The difference between the reference input $v_{ref}(s)$ and the voltage sensor output $H_v(s)v_o(s)$ is called the error signal $v_e(s)$. The objective is to make $v_e(s)$ as small as possible, so that $v_o(s)$ accurately follows $v_{ref}(s)$ regardless of disturbances or component variation in the compensator, pulse width modulator, gate driver, or converter power stage. In practice, the error signal is usually nonzero but nonetheless small. The voltage regulator $G_{c1}(s)$ output is $v_e(s)G_{c1}(s)$ and that represent the current reference signal. If the regulator gain $G_{c1}(s)$ is large enough in magnitude, then a small error signal $v_e(s)$ can produce the required reference current. The whole procedure is repeated for the inductor current with current regulator $G_{c2}(s)$. The current regulator adjusts the duty cycle d(s) as necessary to obtain the desired output voltage.

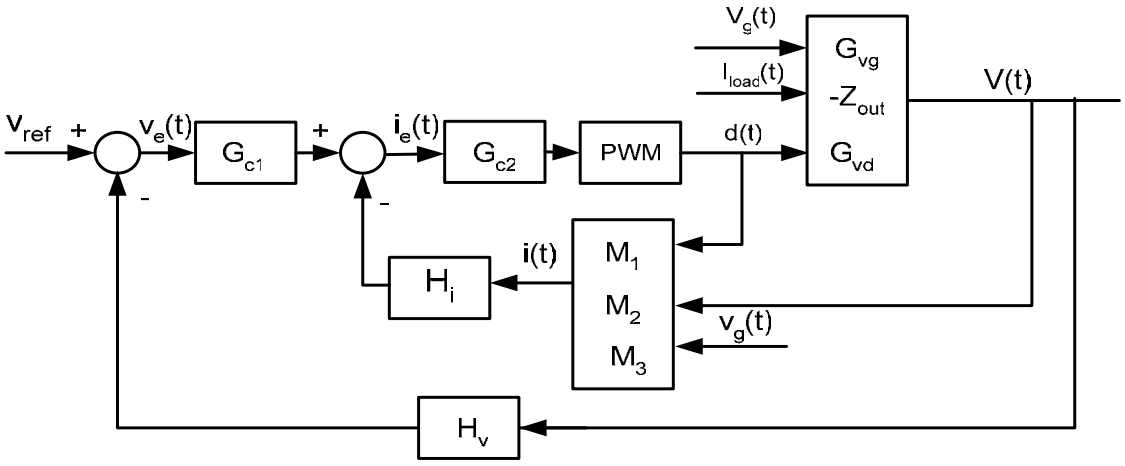

Fig. 39. Detailed control diagram of the boost converter control subsystem.

The inductor current is obtained according to Figure 36 as:

$$i = \frac{1}{sL} v_g - \frac{2-D}{2sL} v_o + \frac{V_o}{2sL} d \tag{52}$$

and corresponding blocks in Figure 39 are:

$$M_1 = \frac{Vo}{2Ls}; \qquad M_2 = \frac{1}{Ls}; \qquad M_3 = -\frac{2-D}{2Ls}. \tag{53}$$

The output voltage variation $v_o(s)$ can be expressed as a linear combination of the three independent inputs using the equations 49, 50 and 51, as follows:

$$v_o(s) = G_{vd}(s)d(s) + G_{vg}(s)v_g(s) - Z_{out}(s)i_{load}(s). \tag{54}$$

Solving the block diagram in Figure 39 for the output voltage $v_o(s)$ yields:

$$\begin{aligned} v_o(s) &= \frac{G_{c1}(s)G_{c2}(s)PWM(s)G_{vd}(s)}{1+T(s)} v_{ref}(s) + \\ &+ \frac{G_{vg}(s) + G_{c2}(s)PWM(s)H_i(s)\left[G_{vg}(s)M_1(s) - G_{vd}(s)M_3(s)\right]}{1+T(s)} v_g(s) + \\ &+ \frac{-Z_{out}(s)(1+PWM(s)G_{c2}(s)H_i(s)M_1(s)}{1+T(s)} i_{load}(s) \end{aligned} \tag{55}$$

with the loop gain given by

$$T(s) = PWM(s)G_{c2}(s)\left[H_i(s)M_1(s) + G_{vd}(s)\left[G_{c1}(s)H_v(s) + M_2(s)H_i(s)\right]\right] \tag{56}$$

The loop gain T(s) is defined as the product of the small-signal gains in the forward and feedback paths of the feedback loop. From the previous equation 55 we can observe that the transfer function from a disturbance to the output is multiplied with the factor 1/(1+T(s)). Hence, when the loop gain T is large in magnitude, then the influence of the disturbances on the output signal is small. A large loop gain also causes the output voltage $v_o(s)$ to be nearly equal to $v_{ref}(s)/H_v(s)$ ($H_i(s)$ very small) with very little dependence on the gain in the forward path of the feedback loop.

The stability is another important issue in feedback systems. It is well known that adding a feedback loop can cause an otherwise stable system to become unstable. And even when the feedback is stable, it is possible for the transient response to exhibit undesirable ringing and overshoot. In-depth discussion of the stability is beyond the scope of this thesis; however, the simple phase margin criterion will be used. If there is exactly one crossover frequency, and if the loop gain T(s) contains no right half-plane poles, then the quantities 1/(1+T) and T/(1+T) contain no right half-plane poles when the phase margin is positive [20].The crossover frequency is defined as the frequency where the magnitude of the loop gain is unity:

$$\left\| T(j2\pi f_c) \right\| = 1 = 0dB \tag{57}$$

and to compute the phase margin φ_m, the phase of the loop gain T is evaluated at the crossover frequency, and 180° is added:

$$\varphi_m = 180^\circ + \angle T(j2\pi f_c). \quad (58)$$

As mentioned earlier, the voltage and current regulators are generally designed to be the PI controllers. The voltage regulator is designed to obtain slower response than the current regulator; otherwise, the current control may be unstable. The PI controller is used to increase the low-frequency loop gain, such that the output is better regulated at the zero frequency and at frequencies well below the loop crossover frequency. Transfer function of the PI regulator is given by:

$$G_c(s) = K_p + \frac{K_i}{s} \quad (59)$$

where K_p is referred to as the proportional gain and K_i is the integration gain. To the extent that the regulator gain can be made arbitrarily large at the zero frequency, the DC loop gain T(0) becomes arbitrarily large. This causes the DC component of the error signal to approach zero. Consequently, the steady state output voltage is perfectly regulated, and the disturbance-to-output transfer function approaches zero at DC.

4.7 Simulation results

In order to test the performance of the control algorithm for all three scenarios, the system was subjected to a load step change from 5 kW to 1 kW while limiting the output power of the fuel cell to 2 kW indicated by the PA signal. The results of the simulations are presented in Figure 40.

During the high power demand period (Figure 40, region I) a part of the load is supplied by the ultracapacitor, which manifests itself as a voltage drop from 80 V to 79.2

V on the ultracapacitor voltage plot. Following the load demand decrease, the fuel cell is able to satisfy the entire load and charge the ultracapacitor at the same time (Figure 40, region II). After the capacitor is fully charged the system enters the normal operation mode (Figure 40, region III) where all requested energy is provided by the fuel cell.

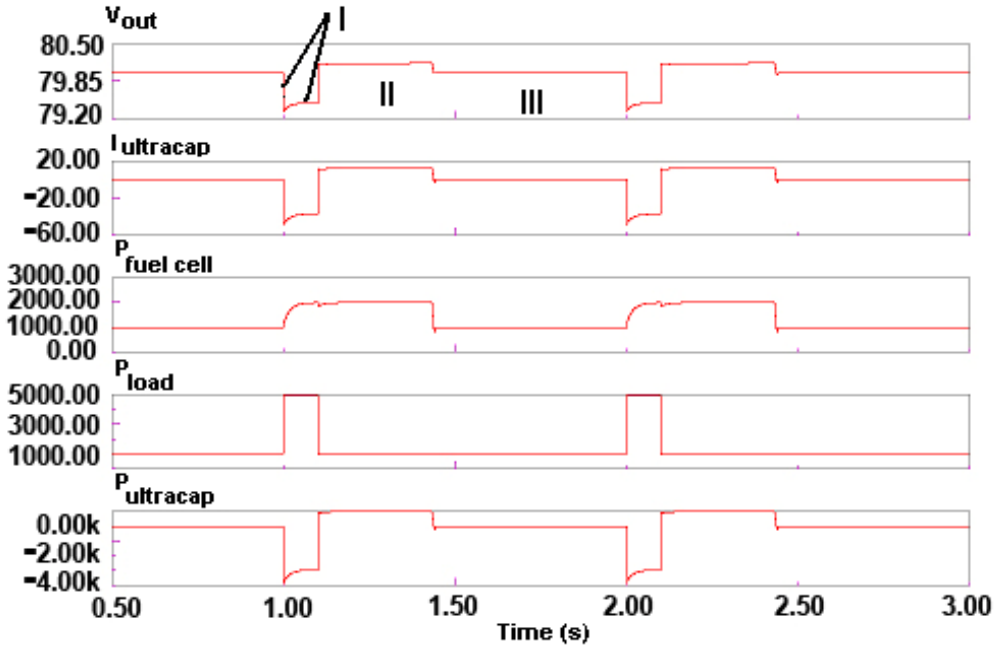

Fig. 40. Ultracapacitor voltage, ultracapacitor current, the power supplied by the fuel cell, load power demand and ultracapacitor power.

Another important case is when the auxiliary device is a battery instead of an ultracapacitor. This system was also simulated for all three scenarios, when it was subjected to a change of load from 5 kW to 1 kW while limiting the output power of the fuel cell to 2 kW indicated by the PA signal. The results of the simulations are presented in Figure 41.

During the high power demand period (Figure 41, region I) a part of the load is supplied by the ultracapacitor, which manifests itself as a significant voltage drop from 80 V to 63 V on the battery voltage plot. Following the load demand decrease, the fuel cell is able to satisfy the entire load and charge the battery at the same time (Figure 41, region II). After the battery is fully charged the system enters the normal operation mode (Figure 41, region III) where all requested energy is provided by the fuel cell.

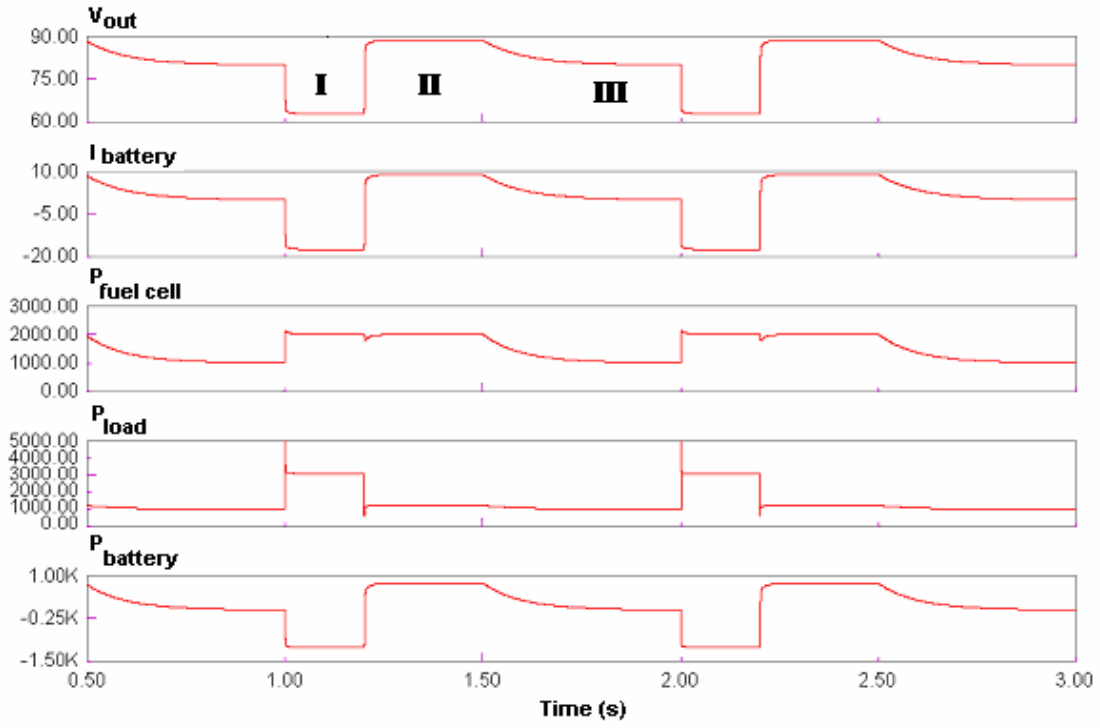

Fig. 41. Battery voltage, battery current, the power supplied by the fuel cell, load power demand and battery power.

4.8 Conclusion

A step-up DC-DC converter topology using three-level boost modules along with a new control strategy has been presented. It has been shown that the primary boosting stage plays the crucial role in the optimal operation of the entire fuel cell conditioner. Consequently, we focused on selecting the most efficient configuration for the primary converter. For the sake of completeness, the basic operations of the secondary two-inductor boost converter and its open-loop control were described briefly. The closed-loop control of the primary Dc-DC converter subsystem was designed using the AC equivalent model and transfer characteristics of the selected topology. The loop gain equations of the converter were derived and the behavior of the output-to-disturbances transfer characteristic and output-to-reference transfer characteristic was analyzed. Also, the stability of the closed loop system was discussed. Simulation results using both the ultracapacitor and battery were shown.

CHAPTER V
EXPERIMENTAL RESULTS

5.1 Design example

The power conditioning unit and the control scheme are designed to interface 5 kW SOFC with the programmable 2 kW DC load. Therefore, the output voltage of the primary DC-DC converter has to be maintained at 80 V. Output of the secondary DC-DC converter has been maintained to 400 V The detailed converter specifications are shown in Table V as follows.

Table V DC-DC converter specifications

Parameter	Value
Input voltage range	42-60 V
Output Power	5 kW
Output Voltage	400 V

The system is designed to operate at 5 kW, which, according to Figure 2, corresponds to the minimum input voltage of 42.3 V. This ensures that the converter is working in only one mode when $V_{in}>V_o/2$ (as previously described), yielding the duty cycle of

$$D = 2 - \frac{2V_{in}}{V_o} = 0.9425. \tag{60}$$

The input current is calculated to be 132.3 A, assuming the full power with 90% efficiency. Considering that the current is high, a selection of the 100 kHz switching frequency reduces the inductor's core size. Assuming the ripple current level of 5%, the needed inductance is

$$L = \frac{V_{in} - 0.5V_{cap}}{2\Delta I} DT_S = 2.87\mu H. \tag{61}$$

Maximum current ratings of switches S_{b1}, S_{b2} and diodes D_{b1}, D_{b2} are calculated to be 66 A and their voltage rating is

$$V_o / 2 = 40V. \tag{62}$$

The resistance of the 5 kW load with the regulated output voltage of 80 V is found to be

$$R = \frac{V_o^2}{P} = 1.28\Omega. \tag{63}$$

The second stage input voltage is regulated by the three-level boost converter to 80V and the output voltage of the converter is to be maintained at 400 V. In this case the transformer turns ratio n_1/n_2 is chosen to be 1/2. Therefore, from equation 64 a duty cycle, which is the overlapping time of the switches S_1 and S_2, is calculated to be

$$D = 1 - \frac{2V_{out}n_1}{V_o n_2} = 0.16. \tag{64}$$

The input current of the converter is calculated from the output power and input voltage considering the efficiency of 90%, and it results to be 32.7 A. The switching frequency of 20 kHz for this stage is used in order to minimize switching losses. Then, given an input current ripple of 5%, the required inductor values for L_1 and L_2 are obtained to be

$$L = \frac{V_o D}{2 f_s} \frac{1}{I_{ripple} I_{in}} = 205uH \tag{65}$$

The maximum ratings of switches S_1 and S_2 are calculated to be 53A peak for the current and their voltage rating is

$$V_{ds} = 2\frac{n_1}{n_2} V_{out} = 400V \tag{66}$$

Similarly the voltage rating of the rectifier switches S'_1 and S'_2 can be calculated to be

$$V_{ds,rec} = 2V_{out} = 800V \tag{67}$$

Finally, their current rating is calculated to be 18 A peak.

The chosen output capacitance is 3 mF and the input inductance is 51 μH. The voltage feedback gain $H_v(s)$ is one and current feedback gain is $H_i(s)=1/Imax=0.00845$.

The pulse width modulator (PWM) is a simple comparator circuit with symmetrical saw-tooth signal generator shown in Figure 42. The PWM transfer characteristic is $PWM(s)=1/V_m$, where V_m represents the amplitude of the saw-tooth waveform and in this example is unity.

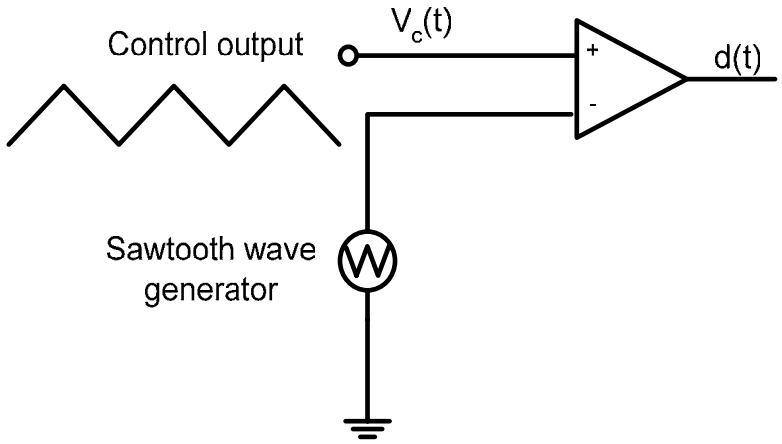

Fig. 42. Pulse width modulator circuit.

The voltage control transfer function is $G_{c1}(s)=k_1+k_2/s$, while the current control transfer function is $G_{c2}(s)=k_3+k_4/s$, where $k_1=0.1$, $k_2=200$, $k_3=10$, and $k_4=50000$. The open loop converter transfer functions are discussed in the previous chapter. The open loop control-to-output transfer function is

$$G_{vd}(s)=G_{d0}\frac{1-\dfrac{s}{\omega_z}}{1+\dfrac{s}{Q\omega_o}+\left(\dfrac{s}{\omega_o}\right)^2} \tag{68}$$

where

$$G_{do}=75.65=37.58dB;\ \omega_z=2\pi\cdot 1116.76\frac{rad}{s};$$

$$\omega_o=2\pi\cdot 304.26\frac{rad}{s};Q=3.67=11.29dB.$$

The line-to-output transfer function is given with:

$$G_{vi}(s) = G_{i0} \frac{1}{1 + \frac{s}{Q\omega_o} + \left(\frac{s}{\omega_o}\right)^2}$$

where (69)

$$G_{io} = 1.89 = 5.53dB;\ \omega_o = 2\pi \cdot 304.26 \frac{rad}{s}; Q = 3.67 = 11.29dB$$

and the output impedance is given by:

$$Zout = \frac{4Ls}{(2-D)^2 + s^2 2LC} = \frac{2.04 \cdot 10^{-4} s}{1.118 + 3.06 \cdot 10^{-7} s^2}. \quad (70)$$

Figures 43-48 show the Bode plots of the open loop transfer characteristics given in equations 68-70.

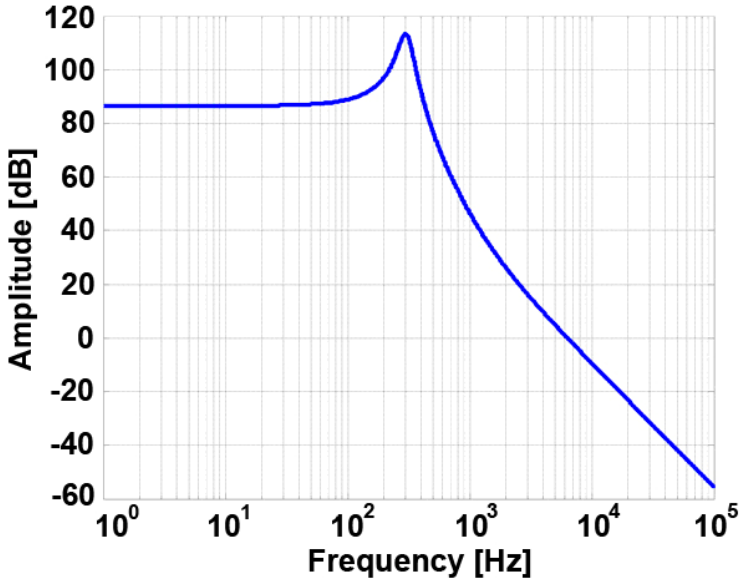

Fig. 43. Amplitude characteristic of the control-to-output transfer function.

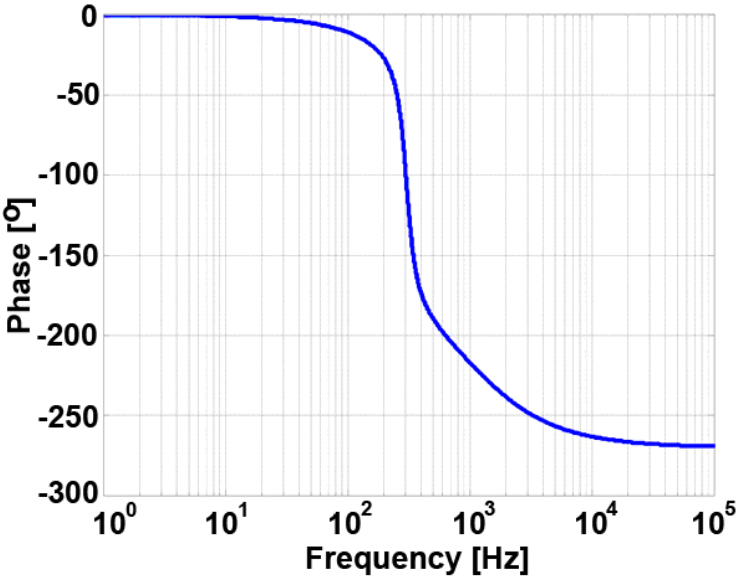

Fig. 44. Phase characteristic of the control-to-output transfer function.

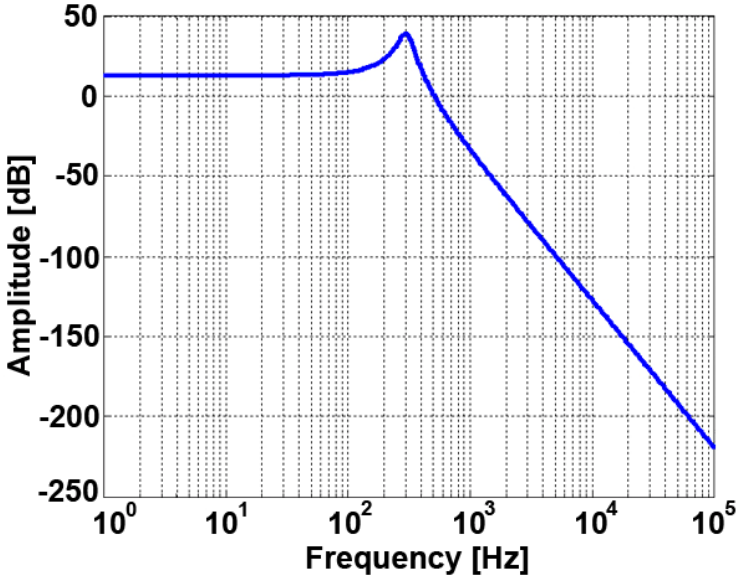

Fig. 45. Amplitude characteristic of the line-to-output transfer function.

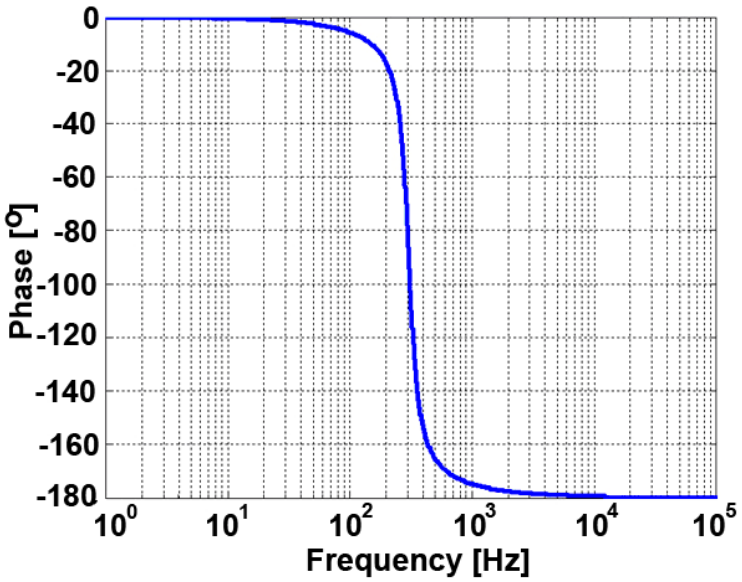

Fig. 46. Phase characteristic of the line-to-output transfer function.

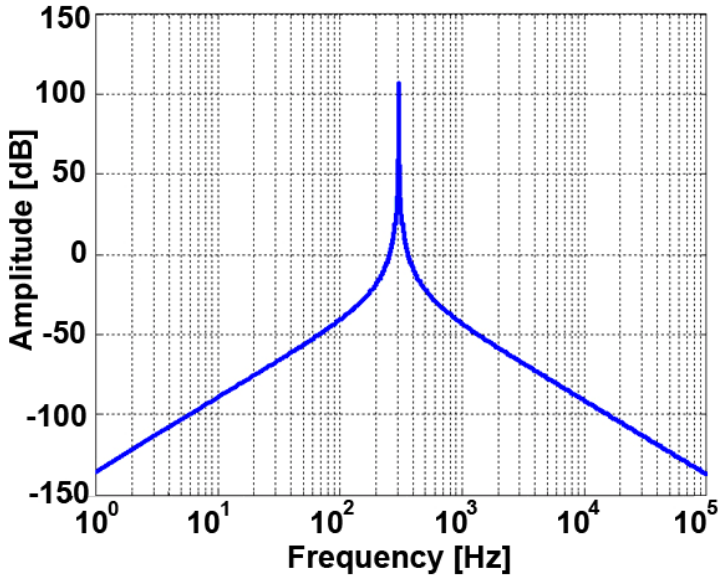

Fig. 47. Amplitude characteristic of the output impedance.

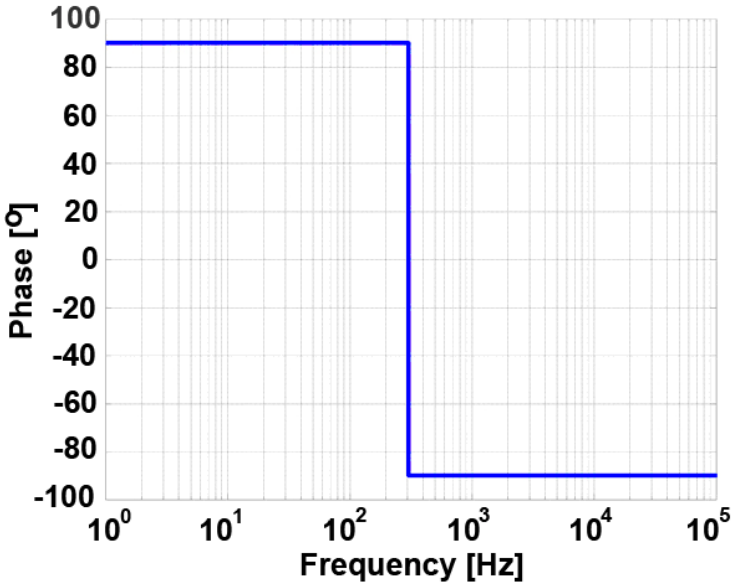

Fig. 48. Phase characteristic of the output impedance.

Using the equations 56 and 68-70 and the block diagram in Figure 39 the resulting loop gain of the complete system can be written as:

$$T(s) = G_{c2}(s)\left[M_1(s) + G_{vd}(s)\left[G_{c1}(s) + M_2(s)H_i(s)\right]\right]. \quad (71)$$

The amplitude characteristic of the uncompensated loop gain $T_u(s)$, with unity compensator gain $G_{c1}(s) = G_{c2}(s) = 1$, is sketched in Figure 49 together with the amplitude characteristic of the compensated gain T(s) to illustrate the differences. The DC gain of the uncompensated loop gain is $T_u(0) = 87$ dB while the DC gain of the compensated loop gain is T (0) = 335.4 dB. The PI compensator increases the loop gain at low frequencies, thus improving the regulation of the output voltage. This causes the DC component of the error signal to approach zero.

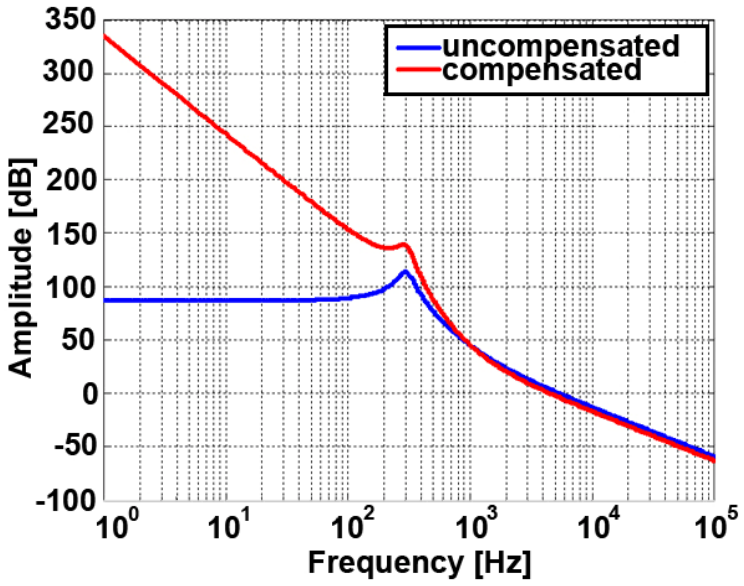

Fig. 49. Amplitude characteristics of the uncompensated and compensated loop gain functions.

The phase characteristic of the uncompensated loop gain $T_u(s)$ is sketched in Figure 50 together with the phase characteristic of the compensated gain T(s). The uncompensated loop gain has the crossover frequency f_c=5.4 kHz, with the phase margin of -74.8 degrees. This shows that the system without the compensator is unstable. The compensated loop gain T(s) does not significantly degrade the bandwidth since it has a crossover frequency of f_c=4.5 kHz; however, with the phase margin of +61.3 degrees, it significantly improves the stability of the system.

In Figure 51 we can see the reference-to-output transfer function, where at low frequencies when ||T|| is large the characteristic shows a desired behavior because it is independent of variations in the gains in the forward path of the loop.

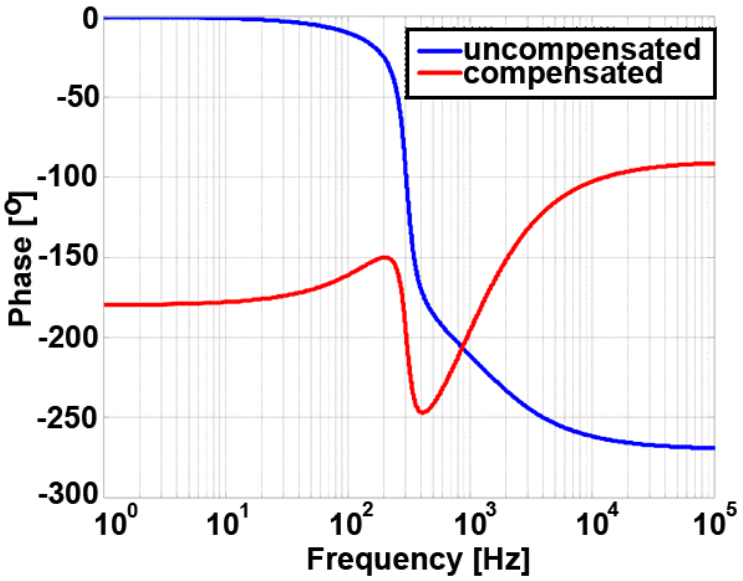

Fig. 50. Phase characteristic of the uncompensated and compensated loop gain functions.

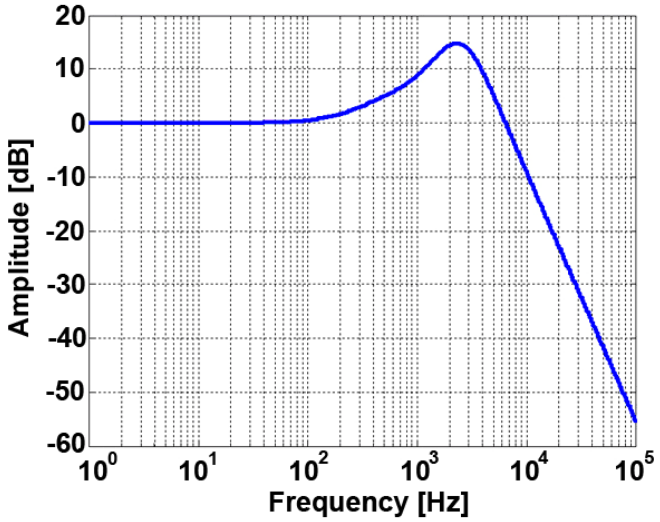

Fig. 51. Amplitude characteristic of the reference-output transfer function.

In Figure 52 we can observe the effect of the feedback loop on the input-to-output transfer function. This transfer function is reduced via feedback by the factor (1+T(s)) as shown in equation 55. Again at low frequencies where ||T|| is large, the disturbances in input signal are reduced greatly.

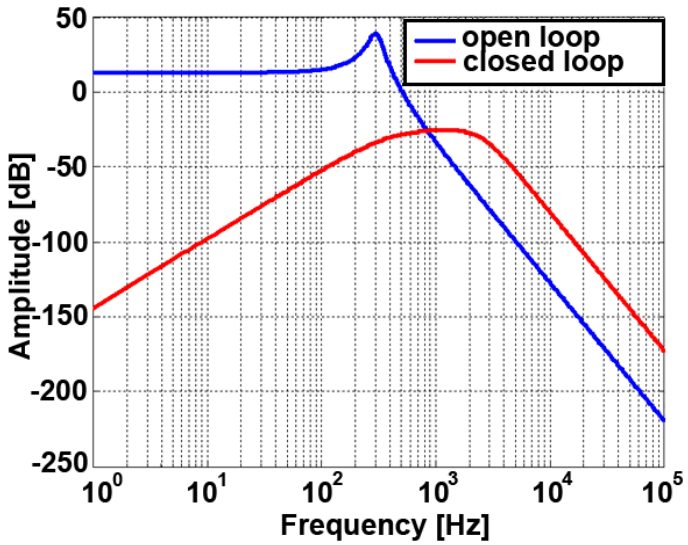

Fig. 52. Amplitude characteristic of the line-output transfer function with open and closed loop.

Similar arguments apply to the output impedance. In Figure 53 we can observe the effect of the feedback loop on the output impedance. This function is reduced via feedback by the factor (1+T(s)) as shown in equation 55. As shown before, at low frequencies where ||T|| is large, the output impedance is reduced greatly in magnitude, while at high frequencies it stayed unchanged.

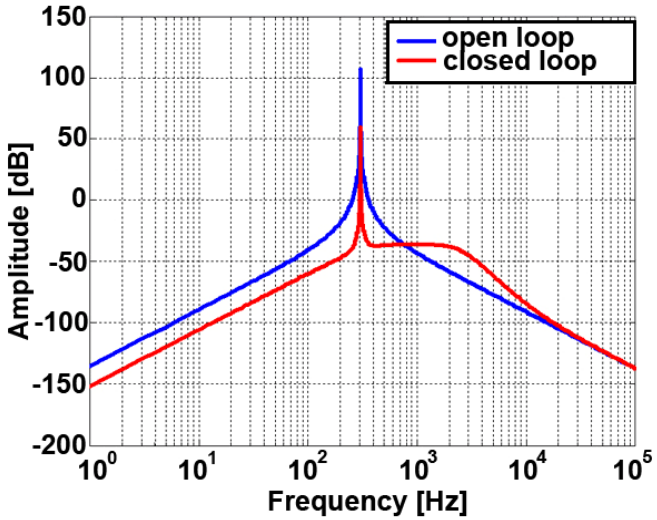

Fig. 53. Amplitude characteristic of the output impedance with open and closed loop.

As a result, we can conclude that the feedback loop can improve the behavior of the system at frequencies below the crossover frequency, but it essentially has no effect on the system's ability to reject the disturbances at the frequencies higher than the crossover frequency.

5.2 Experimental results

The proposed converter and the control algorithm were implemented in a laboratory prototype. The results shown in the following figures correspond to a 2.5 kW prototype

with the switching frequency of 100 kHz. Figures 54-57 correspond to the system with the battery as the auxiliary device, while figures 58-61 correspond to the system with the ultracapacitor as the auxiliary device.

The equivalent battery consisted of 7 individual units (Universal Battery, model UB12180) with the nominal voltage rating of 12 V and equivalent serial resistance (ESR) of 140 mΩ. The ultracapacitor bank consisted of 7 units (KBI KAPower, model 700012) with the operating voltage window of 4-14.5 V and with the individual capacitance of 2000 F. To implement the control system, a fixed-point digital signal processor (Texas Instruments, model TMS320LF2407A [26]) was used. A programmable DC load (Chroma, model 63202) was used in the dynamic current mode to generate the periodic output current with period of 4 s and duty cycle of 0.1. The nominal current level was 10 A and during the short intervals (0.4 s) it increased to 25 A. With the output voltage set to 80 V, this change in the current values corresponds to the power change from 800 W to 2 kW. The current limit was set to 20 A.

Figures 54-57 show the behavior of the system with the ultracapacitor as the auxiliary device. In Figure 54 the input voltage, the input current, the output (ultracapacitor) voltage and the load current are presented. The ultracapacitor current shown in Figure 55 follows the opposite sign convention than the one used in simulations; hence, it is an inverted image of the simulated current. In the same Figure 55, the output voltage and the load current are repeated for easier comparison. Figures 56 and 57 show the input voltage, current and power and the output voltage, current and power, respectively.

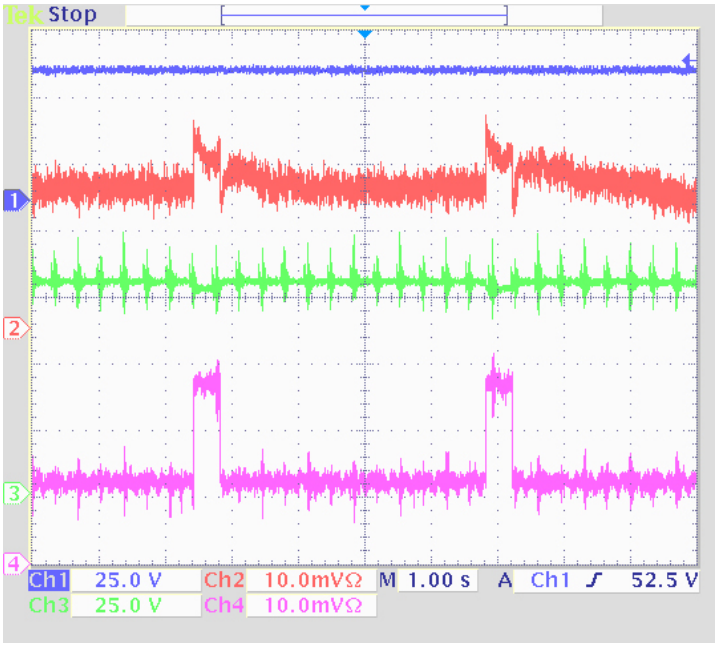

Fig. 54. Input voltage, input current, output voltage and output current with ultracapacitor as the auxiliary device.

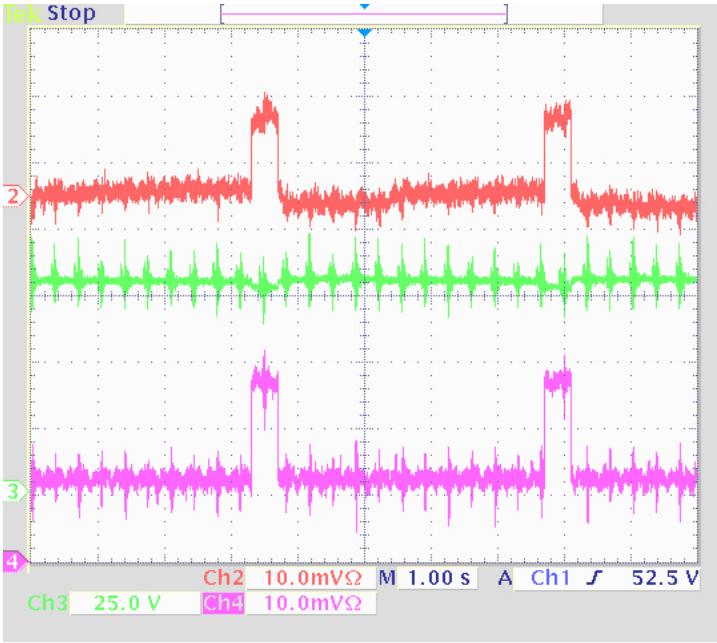

Fig. 55. Output voltage, battery current and output current with ultracapacitor as the auxiliary device.

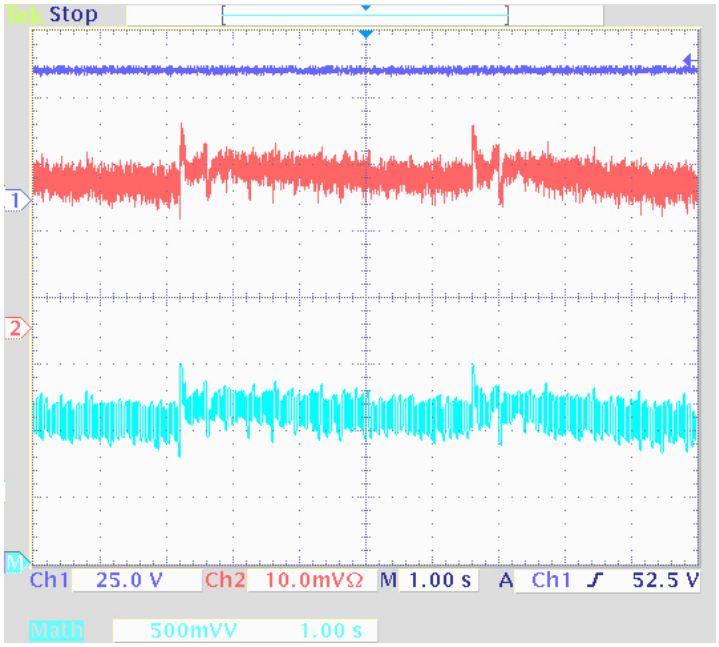

Fig. 56. Input voltage, input current and input power with ultracapacitor as the auxiliary device.

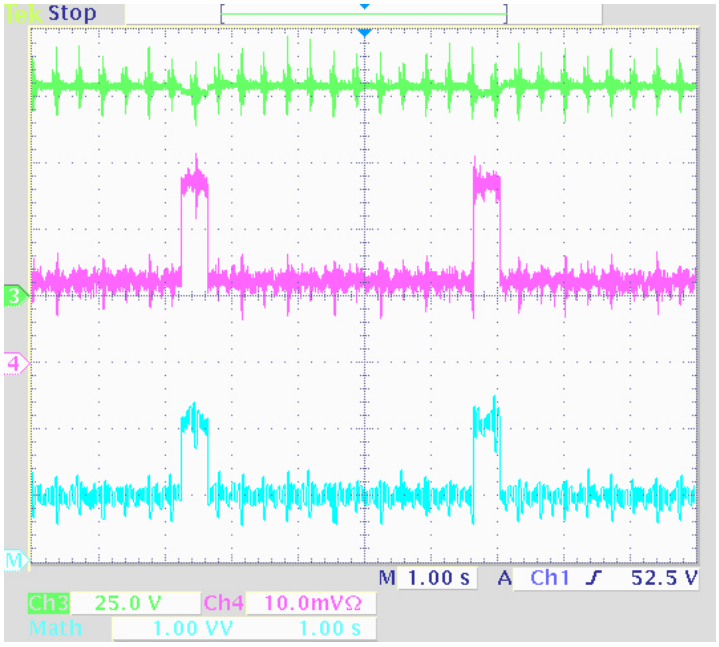

Fig. 57. Output voltage, output current and output power with ultracapacitor as the auxiliary device.

The experimental results are in agreement with the simulation results and all three possible scenarios are presented. During the high power demand period a part of the load is supplied by the ultracapacitor, which manifests itself as a voltage drop from 80 V to 75 V on the ultracapacitor voltage plot (middle waveform in Figure 55). The ultracapacitor current (top waveform in Figure 55) is supplying a part of the load demand. Following the load demand decrease, the input source is able to satisfy the entire load and charge the ultracapacitor at the same time; the ultracapacitor current is below the steady state level, which means it charges the ultracapacitor. After the capacitor is fully charged the system enters the steady state where all requested energy is provided by the input source and the ultracapacitor current is zero.

Figures 58-61 portray the behavior of the system with the battery as the auxiliary device. In Figure 58 the input voltage, the input current, the output (battery) voltage and the load current are presented. The battery current shown in Figure 59 follows the opposite sign convention than the one used in simulations; hence, it is an inverted image of the simulated current. The output voltage and the load current are repeated for easier comparison. Figures 60 and 61 represent the input voltage, current and power and the output voltage, current and power, respectively. The experimental results are in agreement with simulation results and all three possible scenarios are presented. Analogous to the ultracapacitor case, during the high power demand period a part of the load is supplied by the battery, this shows as a voltage drop from 80 V to 60 V on the battery voltage plot (top waveform in Figure 59). The battery current (middle waveform in Figure 59) is supplying a part of the load demand. Following the load demand decrease, the input source is able to satisfy the entire load and charge the battery at the

same time; the battery current is below the steady state level which means it charges the battery. After the battery is fully charged the system enters the steady state where all requested energy is provided by the input source and the battery current is zero.

From the waveforms in Figures 58 and 60, we can observe that the output voltage experiences a big drop from 80 V to 60 V during the high load demand because the battery has a much higher ESR than the ultracapacitor.

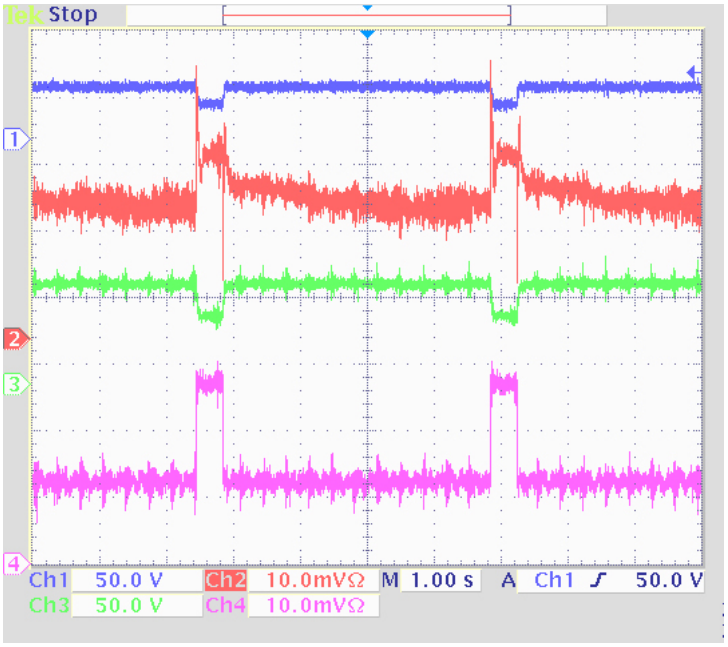

Fig. 58. Input voltage, input current, output voltage and output current with battery as the auxiliary device.

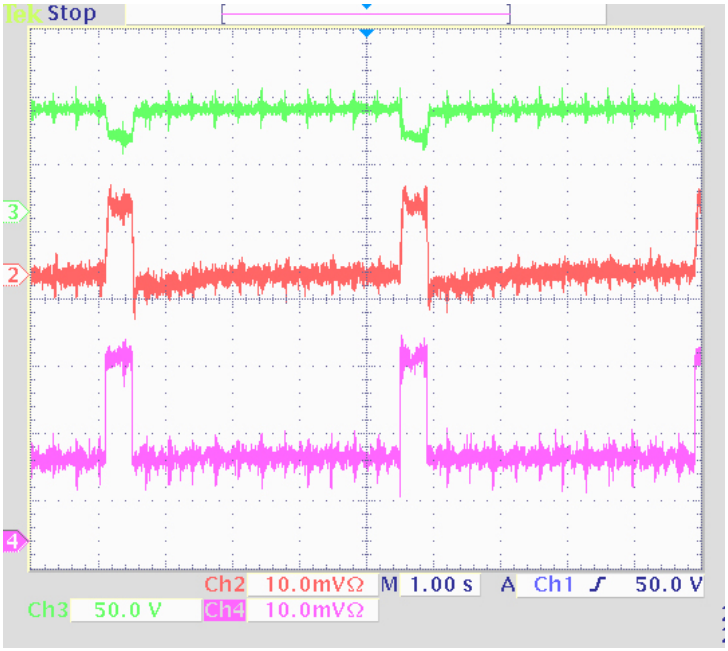

Fig. 59. Output voltage, battery current and output current with battery as the auxiliary device.

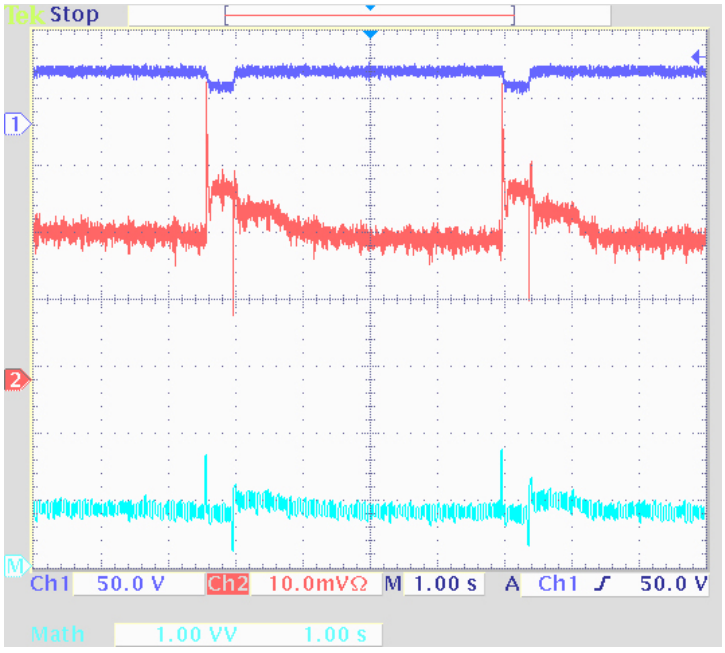

Fig. 60. Input voltage, input current and input power with battery as the auxiliary device.

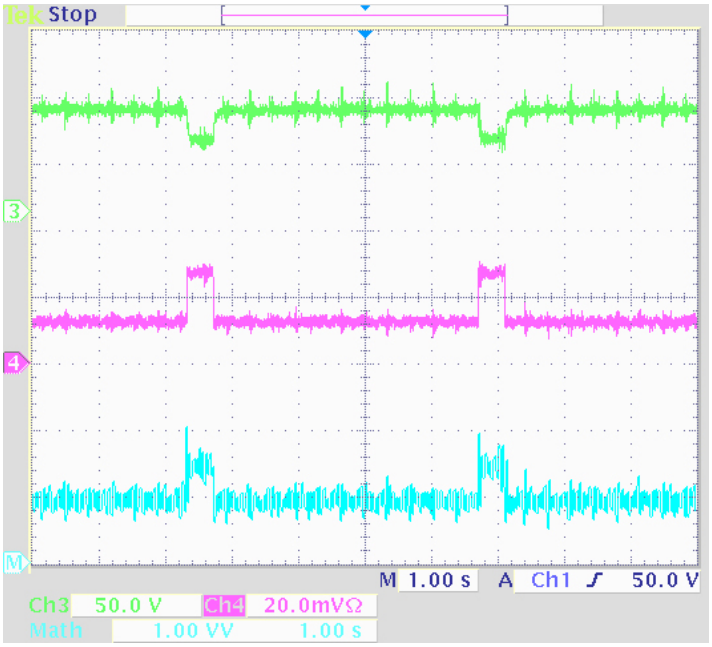

Fig. 61. Output voltage, output current and output power with battery as the auxiliary device.

As observed in simulations and experimentally confirmed there is a significant difference in the system's dynamics in experimental waveforms between configurations with the ultracapacitor and the battery.

The results shown in the following figures correspond to a preliminary 1kW prototype with a switching frequency of 75 kHz. Figure 62 shows the drain to source voltages for switches S_1 and S_2 of the dc-dc converter when supplying a 750 W load under steady state operating conditions. The input voltage of the system during this test was measured to be 40 V, and the input current of the system was measured to be 22 A.

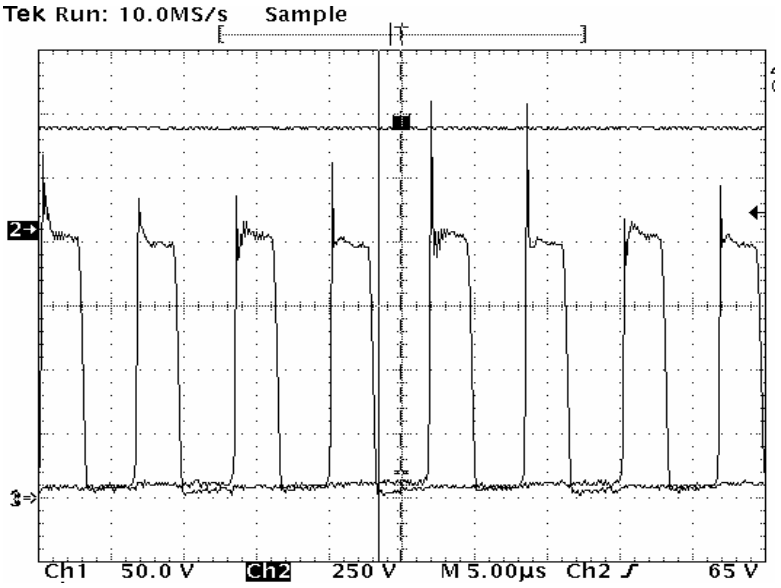

Fig. 62. Converter waveforms for a 750 W output power.

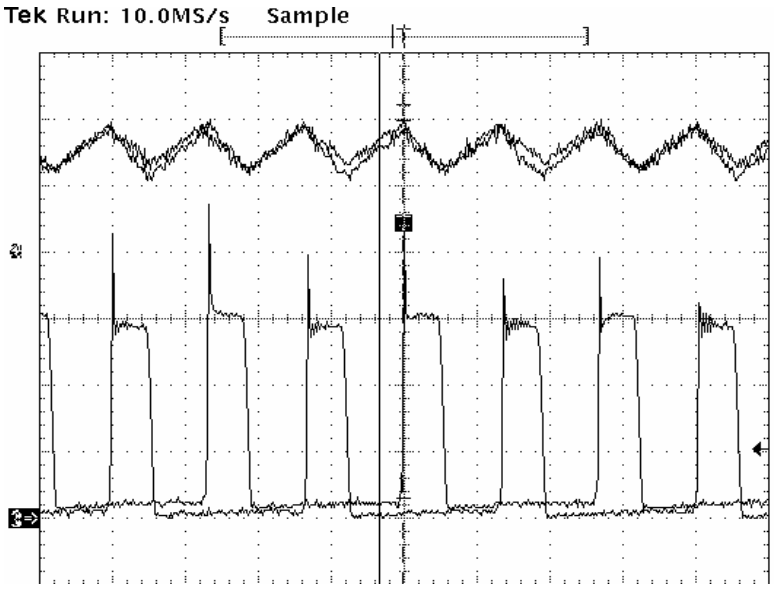

Fig. 63. Current in the coupled inductor T_1.

Figure 63 shows the current waveforms measured in the coupled inductor T1. As can be seen, two currents in the inductors L_1 and L_2 in T1 match perfectly thus reducing the

possibility of saturation in the transformer T_2 due to a current mismatch in the primary winding.

Also from the source to drain waveforms shown in Figures 62 and 63 it can be observed that the voltage stress applied to switches on the primary side of the isolated two inductor boost converter does not exceed 0.5 times the voltage across the switch. This reduces the possibility of device failure due to an over voltage.

As the final result, the efficiency of the three-level boost converter is shown in Figure 64. The efficiency was measured for the output power levels between 0 and 2 kW. It can be seen that the efficiency is practically independent of the power level and is above 90%.

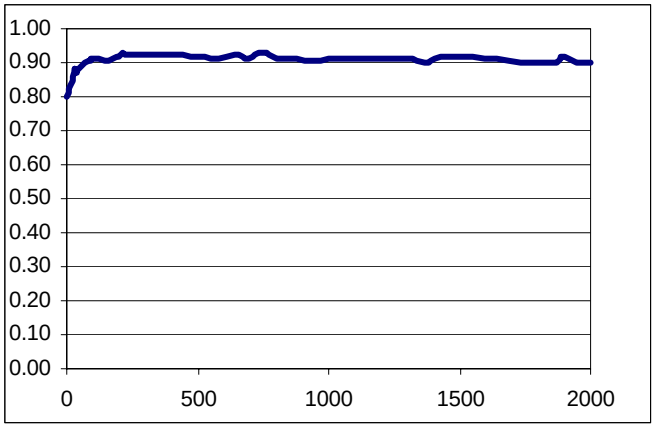

Fig. 64. Efficiency of the three-level boost converter.

5.3 Conclusion

Chapter V focused on the actual design of the parallel three-level boost converter and the two-inductor boost converter that are used as the primary and secondary stages of the fuel cell power conditioner, respectively. Again, the emphasis was placed on the primary boosting stage because of its importance for the performance of the entire system. The

components' values were calculated based on the presented design specifications. Following this, the control system's transfer characteristics, theoretically introduced in Chapter IV, were plotted using Bode plots. It was shown that the introduction of the PI controllers enhances the stability of the system by increasing the phase margin of the compensated transfer functions.

The experimental results were in agreement with the simulation results presented in the previous chapter and show that the system has a good performance and proper response under different load characteristics. More importantly, the power limiting characteristic of the control scheme gives time to the fuel cell to react on its own dynamics when a sudden load increase is applied to the system. As expected, the ultracapacitor proved to be the superior candidate for the auxiliary device due to its faster response to sudden power demands and its lower ESR.

CHAPTER VI
CONCLUSIONS

6.1 Summary

Fuel cells can convert a remarkably high proportion of the chemical energy in a fuel to electricity. With the efficiencies approaching 60%, even without co-generation, fuel cell power plants are nearly twice as efficient as conventional power plants. Unlike in the large steam plants, the efficiency is not a function of the plant size for the fuel cell power plants. Small-scale fuel cell plants are just as efficient as the large ones, whether they operate at full load or not. Fuel cells contribute significantly to the cleaner environment; they produce dramatically fewer polluting emissions, and their by-products are primarily hot water and carbon dioxide in small amounts. Because of their modular nature, fuel cells can be placed at or near load centers, resulting in savings in transmission network expansion. As a result, the fuel cell systems are increasingly used for various purposes, such as in automotive, residential, and industrial applications. Chapter II was dedicated to reviewing the properties of several types of fuel cells.

In order to efficiently use the energy provided by a fuel cell, a typical system requires the use of a conditioner. These fuel cell conditioners consist of a DC-DC converter coupled with a DC-AC inverter to produce the AC waveforms suitable for residential or industrial applications. Chapter III presented a detailed overview of a broad range of DC-DC converters. Important parameters, such as the total active stress on semiconductor components and active switch utilization of the topology, were presented for each configuration and used for the comparison between them.

There is no ultimate DC-DC converter perfectly suited for all applications. For a given application with given specifications, trade off studies should be performed to select the converter topology. Several approaches that meet the specifications should be considered, and for each approach important quantities such as worst case semiconductor device rms currents, size, component count, etc. should be computed. This type of quantitative comparison can lead to the selection of the best converter topology. Driven by this idea, a selection of the most suitable converter topology for the residential use was carried out in Chapter IV. A step-up DC-DC converter topology using three-level boost modules along with a new control strategy has been presented. It has been shown that the primary boosting stage plays the crucial role in the optimal operation of the entire fuel cell conditioner. The closed-loop control of the system was designed using the AC equivalent model and transfer characteristics of the selected topology. The simulation results showed that the system has a good performance and proper response under different load characteristics. More importantly, the power limiting characteristic of the control scheme gives time to the fuel cell to react on its own dynamics when a sudden load step is applied to the system.

Chapter V focused on the actual design of the parallel three-level boost converter that was used as the primary stage of the fuel cell power conditioner. The components' values were calculated based on the presented design specifications. Following this, the control system's transfer characteristics, theoretically introduced in Chapter IV, were plotted using Bode plots. It was shown that the introduction of the PI controllers enhanced the stability of the system by increasing the phase margin of the compensated transfer functions. The experimental results were in agreement with the simulation results and

showed that the system has a good performance and proper response under different load characteristics. As expected, the ultracapacitor proved to be the superior candidate for the auxiliary device due to its faster response to sudden power demands and its lower ESR. The efficiency plot of the three-level boost DC-DC converter has shown that the efficiency was constantly above 90% regardless of the load power demand.

6.2 Future research

The future improvements of the system will involve the use of synchronous rectifiers instead of diodes to further increase the efficiency of the converter. The converter will be tested with the real fuel cell system as the input source instead of the fuel cell simulator. The results shown in Chapter V correspond to a 2.5 kW prototype, while the original target was a 5 kW converter. Next step in the system development will be the making of the 5 kW prototype. That will include the paralleling of two exactly the same converters, which will provide higher output power and boost the overall efficiency.

REFERENCES

[1] J. Gangi, Worldwide Fuel Cell Installations, updated July 2004. [On-line]. Available: http://www.fuelcells.org/info/charts/FCInstallationChart.pdf.

[2] Ballard Power System Inc., Ballard Portable Fuel Cell Generator AirGen, 2003. [On-line].
Available: http://www.ballard.com/resources/powergen/airgenspecsheet.pdf.

[3] Honda, Honda Accord Hybrid: Honda's Best-Selling Vehicle Goes Hybrid, June 2004. [On-line].
Available: http://hondanews.com/CatID2003?mid=2004062848444&mime=asc.

[4] Toyota, Environment, Technology, How Fuel-Cell Hybrid Vehicles Works. Accessed: September 2004. [On-line].
Available: http://www.toyota.com/about/environment/technology/fuelcell2.html.

[5] M. Cropper, Fuel Cell Market Survey, September 2002. [On-line]. Available: http://www.fuelcelltoday.com/FuelCellToday/FCTFiles/FCTArticleFiles/Article_509_MarketSurveyPortableApplications.pdf.

[6] UTC Fuel Cells, New York Power Authority to Install Eight UTC Fuel Cells PC25TM Power Plants at New York City Locations, December 2001. [On-line]. Available: http://www.utcfeulcells.com/news/archive/2001-12-19.shtm.

[7] EG&G Technical Services, Inc., *Fuel Cell Handbook* (sixth edition), Morgantown, WV, US Department of Energy, Office of Fossil Energy, 2002.

[8] K. Wang, C. Y. Lin, L. Zhu, D. Qu, F. C. Lee and J. S. Lai, "Bi-directional DC to DC converter for Fuel Cell Systems," in *Power Electronics in Transportation Conf. Rec.*, October 1998, pp. 47-51.

[9] M. Pagano and L. Piegari, "Electrical Networks Fed by Fuel-Cells for Uninterruptible Electrical Supply," in *ISIE 2002 Conf. Rec.*, vol.3, May 2002, pp.953-958.

[10] C. Liu, T. Nergaard, L. Leslie, J. Ferrell, X. Huang, T. Shearer, J. Reichl and J.Lai, "Power Balance Control and Voltage Conditioning for Fuel Cell Converter with Multiple Sources," in *IEEE PESC 02 Conf. Rec*., vol. 4, June 2002, pp. 2001-2006.

[11] L. Bertoni, H. Gualous, D. Bouquain, D. Hissel, M. C. Pera and J. M. Kauffmann, "Hybrid Auxiliary Power Unit (APU) for Automotive Applications," in *Vehicular Technology Conf. Rec.*, vol.3, September 2002, pp.1840-1845.

[12] G. K. Andersen, C. Klumpner, S. B. Kjaer, and F. Blaabjerg, "A New Green Power Inverter for Fuel Cells," in *IEEE PESC 02 Conf. Rec*., vol. 2, June 2002, pp. 727-733.

[13] G. Scheible, H. Solmecke and D. Hackstein, "Low Cost Soft Switching DC-DC Converter with Autotransformer for Photovoltaic Hydrogen Systems," in *IECON 97 Conf. Rec*., vol. 2, November 1997, pp. 780-785.

[14] M. Hernando, P. Villegas, A. Fernandez, J. Sebastian and J. Corral, "Design Consideration for a 48VDC to ±400VDC Converter for UPS Applications," in *IEEE PESC 03 Conf. Rec*., vol. 4, June 2003, pp. 1924-1928.

[15] 3M Worldwide, 3M Membrane Electrode Assembly (MEA), 2004. [On-line]. Available: http://www.3m.com/about3m/technologies/fuelcells/our_prod.jhtml

[16] K. Kordesch, J. Gsellmann and B. Kraetschmer, "AFC Performance" in *Power Sources 9*, J. Thompson, Ed., New York, NY, Academic Press, 1983.

[17] "Advanced Water-Cooled Phosphoric Acid Fuel Cell Development, Final Report," Report No. DE/MC/24221-3130, International Fuel Cells Corporation for U.S. DOE under Contract DE-AC21-88MC24221, South Windsor, CT, September 1992.

[18] R. Huff, "Status of Fuel Cell Technologies," 1986 Fuel Cell Seminar, October 26-29, 1986, Tucson, AZ, 1986.

[19] N. Minh, "SECA Solid Oxide Fuel Cell Program," in *Proceedings of the Solid State Energy Conversion Alliance 3rd Annual Workshop*, March 2002, [on CD].

[20] R.W.Ericson and D. Maksimovic, *Fundamentals of Power Electronics*, Norwell, MA, Kluwer Academic Publishers, 2001.

[21] M. Pagano, and L. Piegari, "Electrical Networks Fed by Fuel-Cells for Uninterruptible Electrical Supply," in *Proceedings of the ISIE*, May 2002, vol. 3, pp. 953-958.

[22] E. Santi, Franzoni, D, Monti, A., Patterson, D., Ponci, F., et al., "A Fuel Cell Based Domestic Uninterruptible Power Supply," in *Proceedings of the APEC*, March 2002, vol. 1, pp. 605 -613.

[23] M.T. Zhang, Y. Jiang, F.C. Lee and M.M. Jovanovic, "Single-Phase Three-Level Boost Power Correction Converter," in *Proceedings of the APEC*, March 1995, vol. 1, pp. 434 -439.

[24] B. Linch and K. Hesse, "Under the Hood of Low-Voltage DC/DC Converters," Texas Instruments Seminar, March 2004. [On-line]. Available: http://www.ti.com/seminar.

[25] J. Yungtaek and M. Jovanovic, "New Two-Inductor Boost Converter with Auxiliary Transformer," in *Proceedings of the APEC*, March 2002, vol. 2, pp. 10-14.

[26] Texas Instruments, *TMS320F/C240 DSP Controllers*, Owensville, MO, 1999.

APPENDIX

Digital control was implemented using the DSP algorithm shown below:

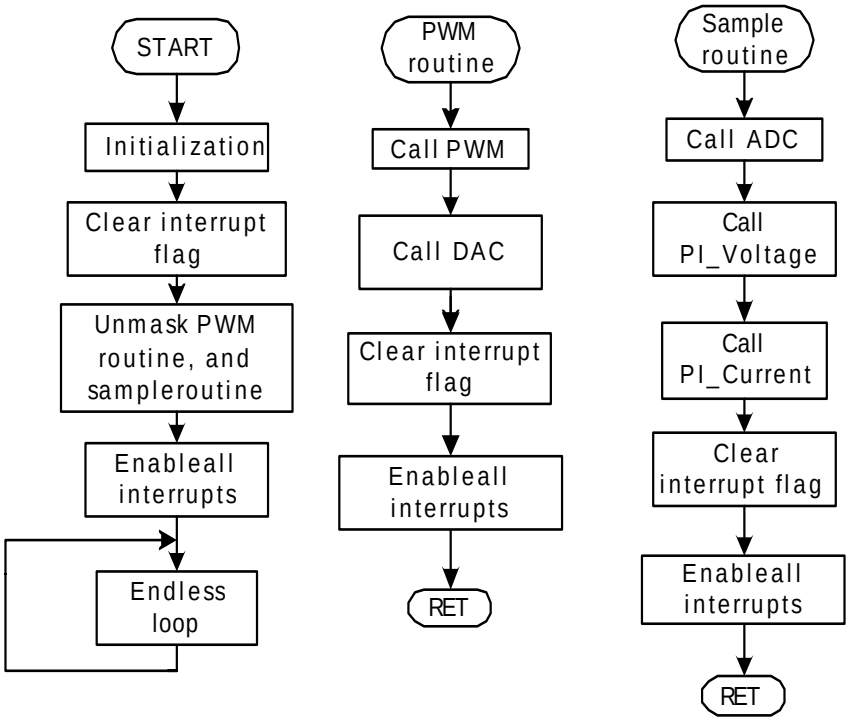

DSP operational flowchart

VITA

Maja Harfman Todorovic graduated with a Bachelor of Engineering (Diploma of Engineering) degree in electrical engineering from the School of Electrical Engineering, University of Belgrade, Belgrade, Serbia and Montenegro in 2001. She joined the master's program in electrical engineering at Texas A&M University in the Fall of 2002, and received her Master of Science degree in December 2004.

Her interests include power electronics, motor drives, energy storage devices, digital control systems and alternative energy applications.

She can be reached at maja@tamu.edu or through the Department of Electrical Engineering, Texas A&M University, College Station, TX 77843-3128.